MTOC clustering and nuclear division through proper spindle positioning in yeast: a microtubule grow-and-catch model

Saptarshi Chatterjee[1], Subhendu Som[1], Neha Varshney[2¤], Kaustuv Sanyal[2], Raja Paul[1*]

1 School of Mathematical and Computational Sciences, Indian Association for the Cultivation of Science, Kolkata -700032, India
2 Molecular Mycology Laboratory, Molecular Biology and Genetics Unit, Jawaharlal Nehru Centre for Advanced Scientific Research, Jakkur, Bangalore -560064, India
¤Current Address: Ludwig Institute for Cancer Research, Department of Cellular and Molecular Medicine, University of California San Diego, La Jolla, CA 92093, USA

* raja.paul@iacs.res.in

Abstract

Mitotic spindle formation in pathogenic budding yeast, *Cryptococcus neoformans*, depends on multitudes of inter-dependent interactions involving kinetochores (KTs), microtubules (MTs), spindle pole bodies (SPBs) and molecular motors. Before the formation of the mitotic spindle, multiple visible microtubule organizing centers (MTOCs), coalesce into a single focus to serve as an SPB. We propose a 'grow-and-catch' model, in which cytoplasmic MTs (cMTs) nucleated by MTOCs grow and catch each other, promote MTOC clustering. Our quantitative modeling identifies multiple redundant mechanisms mediated by cMT-cell cortex interactions and inter-cMT coupling, facilitating MTOC clustering within the experimental time frame. Implementing a similar stochastic model in mitotic spindle where MTs 'grow-and-catch' KTs, we demonstrate that impaired error correction leads to an erroneous partitioning of chromosomes between mother and daughter cells with equal proportions. However, either a marginal delay in the MT nucleation from the SPB of daughter bud (dSPB) or an enhanced MT nucleation from the SPB in mother (mSPB) needs to account for asymmetric chromosome segregation, as observed in Ipl1 depleted cells. Using an analytical model screen, we predict plausible mechanistic conditions for proper spindle positioning. We find that MT buckling together with dynein pull and cortical push maintains proper spindle localization.

Author summary

Cells actively self-assemble bipolar spindle to facilitate chromosomal segregation. In the semi-open mitosis of budding yeast *Cryptococcus neoformans*, before spindle formation, multiple MTOCs embedded on the outer nuclear envelop cluster into a single SPB. The SPB duplicates and organizes spindle, positioning within the daughter bud near the septin ring during anaphase. A mechanistic understanding of MTOC clustering, spindle positioning and chromosomal division in *C. neoformans* are discussed in coherence with experiments. Our computational MT 'grow-and-catch' model identified possible redundant mechanisms for timely MTOC clustering via (a) minus-ended motors crosslinking and sliding anti-parallel cMTs from different MTOCs on the nuclear envelop and (b) biased cMTs (Bim1-mediated) sliding along cortex toward septin ring pull MTOCs in presence of suppressed dynein activity. Using an analytical model and stochastic MT dynamics simulations, we screened various MT-based forces to detect steady spindle positioning. Screening results reveal that proper spindle positioning near the septin ring requires MT buckling from the cell cortex. Furthermore, using an extended model with stochastic MT-KT interaction, we predict that impaired MT nucleation from SPB in daughter together with error correction defects leads to unequal chromosomal division.

Introduction

Spatio-temporal dynamics of organelle-constituents relies primarily on the active organization of microtubules (MTs). MTs are semiflexible polymeric filaments having rapidly polymerizing plus ends and slowly polymerizing minus ends. The growth and shrinkage of MTs are governed by intrinsic dynamic instability parameters [1]. In animal cells, the centrosome is a major MT nucleating center which leads to the formation of a radial MT array [2–4]. However, the radial spanning of MTs in many noncentrosomal MT networks is governed by various membrane organelles such as the Golgi apparatus [2, 5–9]. The cellular structures that harbor the ability to nucleate MTs and organize a radial network are often referred to as Microtubule Organizing Centers (MTOCs) [2, 10].

In the ascomycete budding yeast *Saccharomyces cerevisiae*, spindle pole bodies (SPBs), embedded on the nuclear envelope (NE) are analogous to centrosomes. The SPBs are enriched with distinct $\gamma-$tubulin receptors that organize the cytoplasmic MTs (cMTs) and nuclear MTs (nMTs) [11, 12]. γ-tubulin encoded by *TUB4*, physically interacts with Spc98, Spc97 to form γ-tubulin complexes (γ-TuSCs). Subsequently, the receptors of γ-TuSc, Spc110, and Spc72 localize γtubulin complexes to the SPBs and form a γ-tubulin ring complex (γ-TuRC). This provides SPBs distinct nuclear and cytoplasmic domains indicating that a single MTOC can accommodate nucleation sites for both cMTs and nuclear MTs (nMTs) [2, 10, 13].

In contrast to *S. cerevisiae*, where the SPB being the only MTOC, there are several MTOCs present in the basidiomycete budding yeast *Cryptococcus neoformans* during interphase [14–16] (Fig 1A, S1 Fig). MTOCs dynamically move toward each other and eventually cluster together to form the mother SPB (mSPB) before SPB duplication (Fig 1A, S1 Fig). In *C. neoformans* self-assembly of MTOCs is orchestrated by MT mediated 'grow-and-catch' (also known as 'search and capture') mechanism [14, 17]. Basic characteristics of the clustering mechanisms are shared across a diverse set of organisms as well as several organelle assemblies (e.g. Golgi assembly and stacking, mitochondrial assembly, multi-centrosomal clustering [18] etc.) and are not necessarily organism specific [8]. The mechanics of the MTOC clustering before the formation of the mSPB in *C. neoformans* remains elusive and deciphering the same experimentally is challenging.

After duplication, SPBs separate from each other to facilitate the formation of the mitotic spindle. The plus ends of cMTs interact with the cell cortex via microtubule-associated proteins (MAPs) and molecular motor proteins to drive the local movement, positioning, and migration of the spindle toward the daughter bud. Proper spindle positioning and its alignment ensure equal segregation of the chromosomal volume [14, 19]. In budding yeast *Saccharomyces cerevisae*, a specific location for the mitotic division is predetermined even before the formation of the spindle [14, 20]. The spindle positioning within a confined geometry with an underlying spatial symmetry can often be mapped onto a centering problem across biological systems. For example, force transduction via the active force generators at the cell cortex leads to the centering of the spindle in HeLa cells. It is followed by symmetric division where the cortical pull is a key contributor in the force balance landscape [21]. Similar spindle localization at the cell center is also observed in *Caenorhabditis elegans* embryo during early prophase [22]. Interestingly, in basidiomycetous budding yeast *C neoformans* the spindle is formed within the daughter cell marked by the bilateral separation of SPBs. Therefore, before the spindle formation, the nucleus migrates toward the daughter bud from the mother [17, 19]. In *S. cerevisiae*, timely nuclear migration toward the mother-daughter bud neck juncture requires directed force generation toward the daughter bud. This directed movement stems from the interplay between dynein pull on the plus ends of the cMTs at the mother and daughter cortex along with Bim1 mediated bias of the cMTs supported by a MyoV based machinery in the mother cell [19]. Our previous study [17] reveals that there is a differential spatial arrangement of dynein puncta across the mother and the daughter cell cortex in *C. neoformans*. In the daughter cell cortex, we observed a single large condensed dynein patch, whereas in the mother cortex dynein puncta are small and distributed over a larger region. This differential spatial organization indicates that a net directed pull from the daughter cell cortex mediated by concentrated dynein molecules in association with Bim1-bias in the mother overrides the opposing pull from the mother cell cortex leading to a net nuclear migration toward the daughter bud. Moreover, the default distributed spatial arrangement of dynein patches in the mother cortex (unlike the highly condensed localized patch in the daughter) further reduces resultant pulling force from the mother cortex.

The stable positioning of the spindle is a crucial determinant of the faithful nuclear segregation. Our earlier experimental findings suggest that the mitotic spindle stabilizes near the septin ring inside the daughter [17]. This spatial configuration poses a natural question: what are the force balance conditions necessary and sufficient for such localization? In experiments, it is challenging to quantitatively estimate or tweak forces on the spindle to test the effect of such perturbation on nuclear segregation in *C. neoformans*. Previously, various force balance models have been used to replicate the observed aspects of spindle dynamics [23–26]. In this study, we explored two kinds

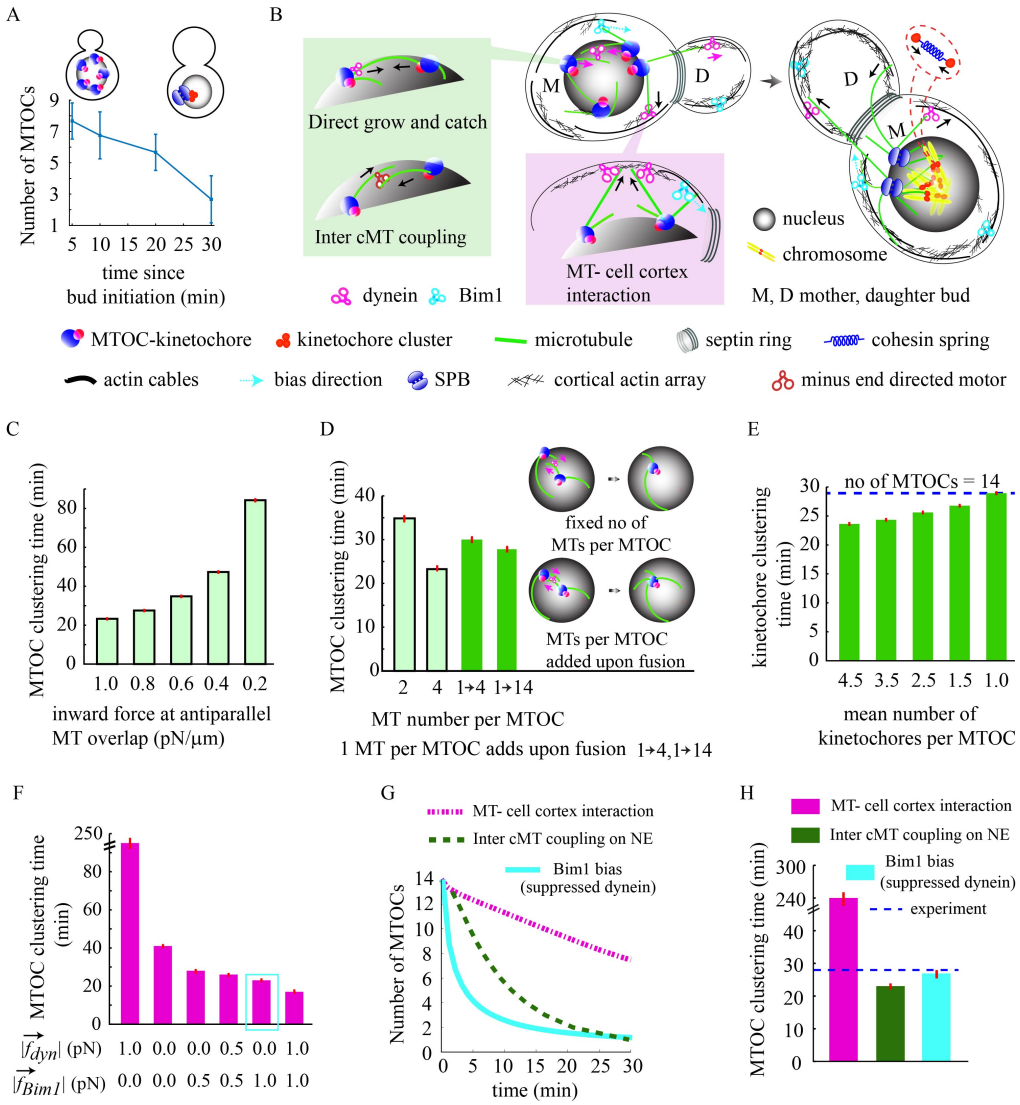

Fig 1. Cooperative interactions among MTs and motors govern MTOC clustering. (A) Number of MTOCs in the cell as a function of time estimated from the bud size. (B) Model schematic depicting MT-mediated grow-and-catch ('search and capture') processes and forces required for the clustering of MTOCs. Arrows indicate the direction of forces. Plausible clustering mechanisms illustrated are: a growing cMT directly catching an MTOC ('direct grow-and-catch'), sliding of anti-parallel cMTs via crosslinking minus end-directed motors on the NE (inter cMT coupling at the NE) and cMT plus-ends interacting with cell cortex (MT-cortex interaction). (C) Clustering time in the sole presence of inter cMT coupling at the NE increases as the minus-ended motor-generated inward force at MT-MT overlap decreases. The MT number is fixed at 4 per MTOC. (D) (First and second bars from left) MTOC clustering time with a fixed number of cMTs per MTOC. Clustering solely via 'inter cMT coupling at the NE' is considered here. (Third bar, $1 \rightarrow 4$) Clustering time when every MTOC nucleates single cMT initially and upon the fusion of the MTOCs the MTs aggregate up to a maximum of 4 cMTs per MTOC. (Fourth bar, $1 \rightarrow 14$) Similar to the "Third bar" but no constraint on the number of cMTs that can add up to the number of MTOCs. (E) Asynchronous assembly of KTs/MTOCs, if more than one KT is associated with a single MTOC. (F) Clustering solely via MT-cell cortex interaction. The clustering is faster when Bim1 bias is enhanced. $|\vec{f}_{dyn}|$ ($|\vec{f}_{Bim1}|$) represents the magnitude of the force generated by a single dynein (Bim1) on each MT at mother cortex. (G) Time progression of MTOC clustering in different mechanisms. The first/fifth bar in Fig 1F denotes the parameter values corresponding to magenta/cyan curve in Fig 1G respectively. (H) Comparison between MTOC clustering timescales via MT-cell cortex interaction, inter cMT coupling on NE and Bim1 bias with suppressed dynein activity at cell cortex ($|\vec{f}_{dyn}| = 0.0$ pN, $|\vec{f}_{Bim1}| = 0.5$ pN). In all figures, sample size n>2000 for simulation and red bars indicate SEM (wherever shown).

of theoretical modeling setup: 1. analytical force balance model, 2. coarse-grained agent-based model. These two models not only complement the primary experimental observations of spindle localization in *C. neoformans*, but reasonably corroborates with each other, qualitatively. In other words, the benchmarking of the analytical model is supported by the agent-based model and vice versa.

Earlier studies indicate that the interdigitated nMTs crosslinked via kinesins and other molecular players initiate the formation of spindle architecture where some of the nMTs actively establish contact with all the kinetochores (KTs) via KT-MT grow-and-catch mechanism [23, 27–31]. It is observed that during budding yeast mitosis, the KTs remain in a 'preclustered' configuration [14, 15, 32]. Accurate chromosome segregation during cell division requires the formation of stable amphitelic attachments, connections between individual sister KTs to opposite SPBs by kinetochore MTs (kMTs) [33, 34]. We developed a similar KT-MT grow-and-catch model to delineate important mechanical conditions for chromosomal segregation in *C. neoformans*.

Based on the experimental observations on MTOC clustering at different stages of the cell cycle, we simulated our agent-based MT 'grow-and-catch' ('search and capture') model to study the clustering of MTOCs into an SPB. We also proposed an analytical model of force balance that replicates proper spindle positioning in *C. neoformans*. Using the model, we investigated the stable position of the mitotic spindle under the combination of various MT mediated forces. In the end, we simulated the KT search and capture by nuclear MTs both in the presence and absence of an error correction mechanism which rectifies erroneous syntelic attachments and explored the conditions for unequal chromosomal segregation.

Taken together, we show that several mechanistic processes can facilitate efficient clustering of MTOCs, either independently or in harness with the other and buckling of cytoplasmic MTs is indispensable for proper spindle positioning. Furthermore, the model reasonably reproduces the defects in chromosome segregation generated due to the impaired error correction mechanism in *C. neoformans* and identifies plausible initial conditions for the emergent aneuploidy.

Results

Developing *in silico* modeling framework

Computational Modeling: We consider the spindle dynamics occurring inside cellular confinement mimicking a budded cell. The mother bud size (radius R_M) is fixed whereas the daughter bud (radius r_D) grows with time. Prior to the SPB formation, all the MTOCs (spheres of radii $r_{MTOC} \sim 0.1$ μm) are embedded on NE (non-deforming spherical nucleus of radius r_{nuc}) and nucleate cMTs. At the onset of the simulation, we considered 14 MTOCs (if not mentioned otherwise) [16, 17]. Each MT is modeled as a cylinder of zero thickness with its length regulated by four dynamic instability parameters (Table 1): catastrophe and rescue frequency (f_c, f_r); growth and shrinkage velocity (v_g, v_s). After complete clustering of MTOCs (S1 Fig, Fig 1A, 1B), mSPB duplicates and nMTs from both the SPBs grow inside the chromosomal volume and catch KTs. Meanwhile, the cMTs that reach the cell cortex, majorly experience instantaneous cortical push ($\vec{F}^{cell-mem}_{push-inst}$), push from the MT buckling ($\vec{F}^{buckle}_{cor}$) and pull due to cortical dynein ($\vec{F}^{dyn}_{cor}$). The cMTs grazing along the NE experience an additional force ($\vec{f}_{overlap}$) at the MT-MT overlap on NE which is proportional to the mean number of minus end-directed motors per unit length (λ_{ovl}) at the overlap. Similarly, forces between KTs and nMTs have been computed (for details, see Material and Methods). The instantaneous positions of all the objects (nucleus, MTOCs, SPBs, KTs) are updated by solving corresponding Stokes equations (Eq. 1-4 in Materials and Methods).

Mathematical Modeling: We formulated a mathematical model to study spindle positioning. We frame the mother and the daughter bud as two intersecting circles of radii R_M and r_D respectively (Table 1). The center of the daughter bud is chosen to be 'd' distance away from the center of the mother. We restrict the spatial movement of the spindle along the line joining the centers, regarded as the axis of symmetry. For simplicity, our analytical model is one-dimensional where all the forces are directed along the axis of symmetry, namely the 'X' axis (S2 Fig). The spindle is chosen to be a rigid rod of length $2a$ with two perfectly bioriented SPBs at its two ends lying on the X-axis. We assume that the cMTs from the SPB facing the mother (daughter) cortex namely $SPB(L)$ ($SPB(R)$), interact solely with the mother (daughter) cortex. We further consider that the cMT length distribution is exponential [23, 35]. Next, we derive closed-form expressions for various MT-mediated forces (instantaneous cortical push, cortical dynein pull, the force due to MT buckling) on the spindle due to MT-cell cortex interaction. The sum of all these forces accounts for the total force on the spindle. The net force balance on the spindle (rigid rod constituting $SPB(L)$ and

$SPB(R)$) determines the spindle position.

In the analytical model, the strength of dynein-mediated pulling is regulated by λ_{dyn}^{M} (Eq. 7-8 in Materials and Methods) and λ_{dyn}^{D} (Eq. 10-11 in Materials and Methods), cortical pushing by A_M and A_D (Eq. 5 and Eq. 6 in Materials and Methods), average MT length by L_{MT}^{av} (Eq. 5-8, Eq. 10-11, Eq. 13-14 in Materials and Methods). In the numerical simulation, the corresponding model parameters are adjusted according to the values listed in Table 1. In most of the cases, the choice of the parameter values is based on the earlier published reports. However, in a few cases, due to the paucity of exact numbers in the literature, the chosen parameter values are optimized for the current study through sensitivity analysis. Below, we present the model investigations exploring MTOC clustering, spindle positioning and chromosome segregation in *C. neoformans*.

Table 1. List of parameters chosen for the model analysis

Abbreviation	Meaning	Value	Reference
R_M	Radius of the mother bud	3 μm	[17]
r_D	Radius of the daughter bud	0.0-2.15 μm	[17]
r_{nuc}	Radius of the nucleus	1.0 μm	[17]
r_{SPB}	Radius of single SPB	0.125 μm	[36, 37]
k_{cor}	Spring constant of the cortex	5.0 pN/μm	[14, 38]
η_{cyt}	Viscosity of cytoplasm	5.0 pN s/μm^2	[14, 38]
η_{nu}	Viscosity of nucleoplasm	10.0 pN s/μm^2	[14, 38]
η_{NE}	Effective viscosity of NE	10.0 pN s/μm^2	[14, 38]
v_g	MT growth velocity	10.4 μm min^{-1}	[17, 39, 40]
v_s	MT shrinkage velocity	28.6 μm min^{-1}	[17, 39, 40]
f_c	Catastrophe frequency of MT	1.0 min^{-1}	[17, 39, 40]
f_r	Rescue frequency of MT	0.02 min^{-1}	[17, 39, 40]
f_c^{stall}	Catastrophe rate of stalled MT	0.04 s^{-1}	[41]
f_{stall}	MT stall force	1.7 pN	[42]
f_{dyn}	Force produced by single dynein	1.0 pN	[43, 44]
f_{Bim1}	Force produced by single Bim1	1.0 pN	[17]
$\lambda_{dyn}^{M(D)}$	Number of dyneins per unit length per MT	6.0 /μm	[45]
λ_{ipMT}	Number of ipMT motors per unit length per MT	1.0 /μm	[38]
λ_{dyn}^{ovl}	Number of minus ended motors per unit length at NE	1.0 /μm	This study
$f_{kinesin-5}$	Force produced by single kinesin-5 motor	1.0 pN	[14]
$K_{cohesin}$	Spring constant of the cohesion springs	0.1 pN/μm	[46]
K_c	Spring constant of KT-kMT connection springs	10.0 pN/μm	[38, 47]
K_{fibril}	Spring constant of the KT fibril	5.0 pN/μm	[38, 47]
D	Euler buckling coefficient	200.0 pN μm^2	[35]
	additional parameters for analytical model		
A_M (A_D)	Instantaneous cortical push amplitude at mother(daughter)	5 pN	This study
B_M (B_D)	Cortical pull amplitude at mother(daughter)	5 pN	This study
D_M (D_D)	Buckling amplitude at mother(daughter)	1000 pN $\times$ μm^2	This study
C_M (C_D)	Steric repulsion amplitude at mother(daughter)	10 pN	This study
ζ_M (ζ_D)	Range of steric repulsion at mother(daughter)	1000	This study
L_{MT}^{av}	Average cMT length	10 μm	This study
a	Spindle half length	1.0 μm	This study
r_D	Radius of the daughter bud	2.15 μm	This study
l_c	Cortex width	0.2 μm	[14]

Clustering of MTOCs progresses via redundant pathways

We have shown previously that all KTs cluster to form a punctum in 25 mins [17]. We have also demonstrated that KTs colocalize with MTOCs [15]. However, the time required for MTOC clustering remains unknown. Now, we validated the time required for MTOCs to coalesce into an SPB by calibrating the clustering time since bud initiation

(time set to zero), in terms of the budding index (S1 FigA, S1 FigB). We observed that since the bud initiation, the daughter bud grows with time, in a reasonably uniform manner, across cells. As the bud growth rate is roughly conserved throughout the cell population, the budding index can be thought of as an intrinsic 'clock' of a budded cell (Fig S1 FigC). The number of MTOCs in cells having similar budding indices (implying that the cells are at the same cell cycle stage) were counted and were plotted with 'time' (calibrated from the budding index) to estimate the MTOC clustering time (Fig 1A). Although electron microscopy suggested as many as 14-16 MTOCs [16], with a limited resolution we could identify a maximum of 8-10 MTOCs in small budded cells.

First, we investigated the MTOC clustering process via MT driven 'grow-and-catch' ('search and capture') on the NE without the cortical interactions. To begin with, we determined the time required for all the MTOCs to cluster if cMTs growing out of MTOCs slide along the NE and directly grow and catch the MTOCs. We considered that in the 'direct grow and catch' mechanism (Fig 1B), the MTs contributing to the clustering process are confined to the NE. As the 'searcher' MT tip nucleated from an MTOC grows (grazes) along the NE and 'catches' another MTOC ('target'), the MTOCs move toward each other along the MT connection until they fuse (Fig 1B). The movement of the MTOCs is strictly restricted to the NE. In this context, we assumed a fixed number of grazing cMTs per MTOC (4 cMTs per MTOC). We found that the timescale for complete clustering achieved by this 'direct grow-and-catch' pathway is significantly large surpassing the relevant mitotic timescales. The MTOCs take ~ 1.5 h to cluster entirely, that too, in ~ 10 % of the population only. The MTOCs fail to cluster into a single focus, in the rest of the population even after ~ 4 hr. Thus, it is unlikely to be an 'efficient' pathway for MTOC clustering. However, the possibility that the same pathway may work in combination with other efficient pathways cannot be ruled out.

Next, we introduced antiparallel sliding amongst the grazing cMTs on the NE (inter cMT coupling, Fig 1B). Inward sliding of the overlapping cMTs from two different MTOCs can be steered by crosslinking minus end-directed motors [48]. The crosslinking activity of minus end-directed motors acting at the MT-MT overlap brings the engaged MTOCs towards each other. In the earlier scenario, a 'searcher' MT has to grow and catch another MTOC. However, in the present context, a 'searcher' MT can grow and catch another MT segment so that the negative end-directed motors can crosslink them and initiate antiparallel sliding. Adding the negative end-directed motor crosslinking and sliding on the NE facilitate the timely clustering; clustering of all the MTOCs (~ 100 %) into a single body happens within ~ 23 min (Fig 1C, S1 Video). As expected, when the inward force between the MTOCs due to negative ended motors diminishes, the net clustering time increases (Fig 1C).

In several models, it has been shown that cellular processes involving MT mediated 'grow-and-catch' mechanisms are often optimized by the regulation of the number of MTs [49, 50]. In a similar 'search and capture' process, as the MT number increases, the capture time gradually decreases to a threshold timescale followed by a saturation [51]; the scenario implies that upon a stepwise increase in the number of MTs per MTOC, the clustering time is expected to decrease. We further investigated the sensitivity to varying cMT numbers in a case by case fashion; a. the MT number per MTOC is kept constant upon clustering of two MTOCs, b. adding the MT number upon a fusion of the MTOCs up to a maximum limit to 4 MTs per MTOC and then, c. removing the maximum limit respectively (Fig 1D).

It was demonstrated earlier that MTOCs colocalize with KTs (Cse4) [15, 52]. Thus, we examined what happens to the KT clustering if one or more KTs are attached to the MTOCs at the beginning (Fig 1E). Our model predicted that if more than one KT is attached to an MTOC, the KT clustering process is marginally faster than the MTOCs.

Next, we explore the role of cMT-cell cortex interaction in the clustering process. There are two major cortex-based forces on the cMTs: a. net pull on the MT segments sliding inside the cortex via the cortical dyneins towards the cortex; b. Bim1 mediated force on the cMTs that have a directional preference towards the septin ring (MT-cell cortex interaction, Fig 1B). We found that the exclusive activity of dynein mediated MT- cell cortex interaction leads to nearly complete clustering of the MTOCs but the time estimated (~ 240 min) is way too high (Fig 1F, S2 Video). However, a decrease in the cortical pull and/or subsequent increase in the Bim1 mediated bias reduces the clustering time scale to $\lesssim 50$ min (Fig 1F, S3 Video). We find that the dynein mediated pull on the MTOCs via cMTs acts in random directions, whereas the Bim1 mediated bias is always directed towards the septin ring. Thus dynein dominated cortical pull suppresses the effective Bim1-bias and delays the clustering. When dyneins are suppressed, due to Bim1-bias all the MTOCs are drifted towards the septin ring while embedded on the NE and cluster.

The time scales for complete MTOC clustering appears to be similar when, a. MTOCs aggregate due to antiparallel sliding of the grazing MTs on the NE via minus ended motors and b. MTOCs aggregate due to diminished cortical dynein pull concomitantly with enhanced Bim1-bias at the cortex (Fig 1G, 1H, Table 2). This highlights an important physical possibility that the clustering mechanisms may be redundant, i.e., the mechanisms either act in liaison or

independently.

Table 2. Various mechanisms of MTOC clustering as examined by the *in silico* model

MTOC clustering	Interactions	Clustering time (min)	% of MTOCs clustered within 25 min
agent based computational model	MT-cell cortex interaction	~ 240	~ 40
	inter cMT coupling at the NE	~ 23	~ 100
	MT-cell cortex interaction with diminished cortical pull and enhanced Bim1 bias	~ 25 [17]	~ 99

The complete clustering of MTOCs into a single body marks the formation of the mature mother SPB followed by SPB duplication. Subsequently, the duplicated SPBs separate into a bi-oriented configuration that initiates spindle formation. In our earlier and present studies, it has been shown that the mitotic spindle stabilizes inside the daughter bud close to the septin ring in *C. neoformans* (Fig 2A) [17]. To understand the stable spindle localization, we propose a simple analytical model, that estimates net force balance on the spindle (See Materials and Methods, S1 Text, S2 Fig). We considered closed-form expressions for various MT-based forces and examined various possibilities of the spindle localization under the combinatory effect of these forces (Fig 2,S2 Fig-S4 Fig).

Balance of cellular mechanical forces guides the spindle position

A spindle is constantly acted upon by molecular forces arising from the interactions of its components with the surrounding [14, 17], e.g., cMTs interacting with the cell cortex via dynein generates a pull on the nucleus toward the cell periphery; similarly, cMTs buckling in contact with the cell membrane pushes the nucleus away from the membrane. These interactions are plausible in both mother and daughter cell cortices. Besides, interactions of cMTs with the septin ring and the cortical actin cables generate an effective bias translating the plus ends of the cMTs toward the daughter bud. Since these forces are spatially inhomogeneous and rapidly varying with time, it is logical to ask how the nucleus and the spindle attain steady positions before the chromosomal segregation.

We formulate an analytical template in one dimension that accommodates all key MT-mediated force contributors originating from the mother and daughter cortices acting on the SPBs (Fig S2 Fig). The mechanistic force balance landscape emerging from the mathematical model allows us to carry out sensitivity analysis across a wide parameter regime constituting a myriad of forces with different characteristics (e.g. instantaneous pushing and buckling of the cMTs, dynein mediated pulling, etc.). From experiments and agent-based simulation, we observe that the average spindle length is ~ 1.5 μm in wild-type (S3 FigA) and the neck to spindle distance is ~ 1 μm while the spindle is in the daughter bud (S3 FigB). Also, the spindle lies almost parallel to the axis of symmetry (orientation angle ~ 15 degree) joining the centers of mother-daughter bud (S3 FigC).

To test how sensitive is the spindle positioning to the cMT-cortex based forces, we introduced instantaneous push and dynein pull from both the mother and daughter cortex. Then, we varied the dynein density in the daughter cortex, keeping the rest of the parameters fixed at base values denoted in Table 1. If the dynein pull from the daughter cortex is too strong, the spindle collapses onto the daughter cortex. In the other limit, the spindle collapses onto the mother cortex, when the cortical pull from the mother cortex overpowers the pull from the daughter (Fig 2B). Thus, in the absence of MT buckling, the spindle localizes at the cortex.

Adding the force due to MT buckling (with two other forces: cortical pull and instantaneous push) restores the stable spindle position near the septin ring (Fig 2C-2D). The spindle robustly maintains its position inside the daughter bud, close to the septin ring upon considerable variation in the average cMT length (Fig 2D, Table 3).

We also tested the spindle positioning in the absence and presence of MT buckling exploiting a three-dimensional agent-based computational model (S3 FigD-S3 FigE). We find that a moderate dynein pull is crucial for the spindle to migrate into the daughter. In the absence of MT buckling, the spindle localizes deep inside the daughter cortex for moderate and strong dynein pull from the daughter (S3 FigD). However, with MT buckling turned 'on', the spindle settles inside the daughter bud and stabilizes close to the septin ring. The spindle distance from the septin ring measured in the experiment (S3 FigB) and estimated from the analytical (Fig 2D) and computational models (S3

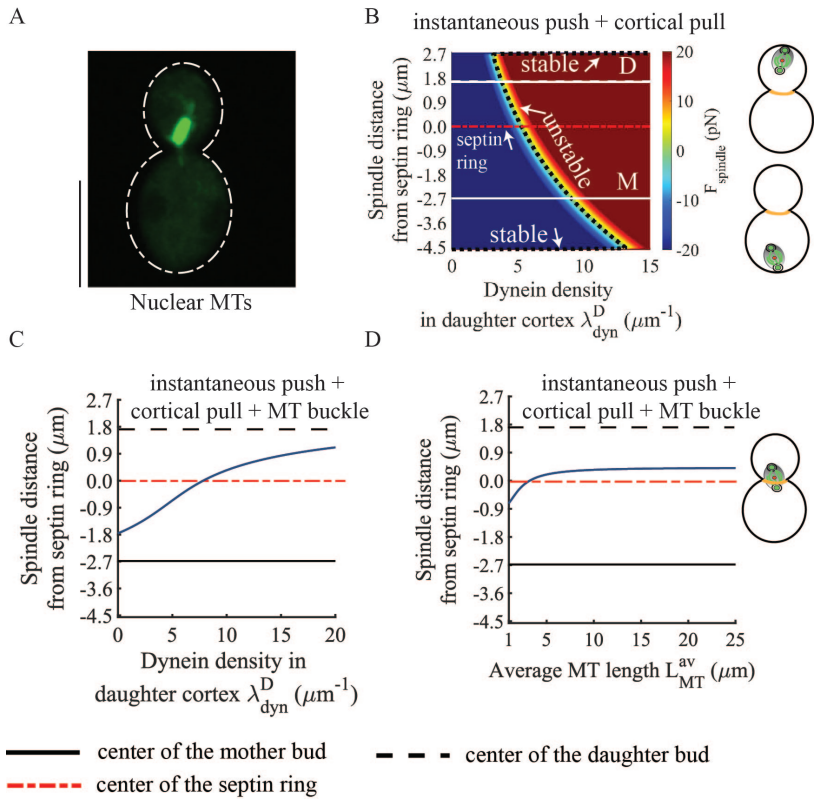

Fig 2. The mechanistic force balance model explains spindle positioning in *C. neorformans*. (A) Microscopic image of nMTs shows spindle position during anaphase in the wild-type cells expressing GFP-Tub1. Bar, 5 μm. (B) Spindle stably collapses onto the cell cortex as dynein density in the daughter cortex (λ^{D}_{dyn}) is varied. Dynein density in the mother cortex (λ^{M}_{dyn}) is fixed and instantaneous cortical push is present in both mother and daughter cortex. Colorbars represent the net force on the spindle and solid lines denote the center of the daughter and mother buds. (C) Step-wise increase in dynein density in the daughter cortex (λ^{D}_{dyn}) moves the spindle into the daughter cortex, localizing near the septin ring when MT buckling is combined with instantaneous push and dynein pull from the cell cortex. (D) Spindle position depending on the variation in average MT length (L^{av}_{MT}). Instantaneous cortical push, dynein pull, and MT buckling are present at both mother and daughter cortex. In plots B-D, -ve/+ve distance refers to the spindle in mother (M)/daughter (D) bud.

FigE, fourth bar) reasonably agree with each other. Interesting spindle characteristics predicted by the model are summarized in the S1 Text, S4 Fig, and Table 3.

Impaired error correction segregates erroneous chromosomes with equal proportions between the daughter cells

The lifetime of a single MT-KT attachment is closely linked with the inter-KT distance and presence of checkpoint protein kinase. Low tension MT-KT attachments, such as syntelic and monotelic attachments undergo degradation owing to the phosphorylation of kinetochore proteins whereas high tension amphitelic attachments are bioriented and stabilized [53]. In the high tension amphitelic attachments, the bioriented configurations are stretched to the extent that their destabilization is minimized. The low tension non-amphitelic attachments, on the other hand, undergo destabilization as their poorly stretched geometric configurations fall under the influence of phosphorylation gradient of the checkpoint proteins preventing aneuploidy. In spindles, where a single MT interacts with a KT, a natural question is how important is the correction of erroneous attachments for equal division of chromosomes into mother and daughter cells? What are the prime factors that influence the unequal division?

We simulated two scenarios: first, the wild-type scenario with error correction mechanism in force; second, the error correction is absent, mimicking Ipl1 depletion (Fig 3A). As the initial KT-MT attachments are formed due

Table 3. Analysis of parameter sensitivity in spindle positioning (analytical model). M, D stand for mother and daughter bud respectively. * Spindle collapsed onto the cell cortex.

instantaneous push	cortical pull	MT buckle	vary	magnitude	spindle position
✓(M,D)	✓(M,D)	✗(M,D)	λ_{dyn}^{D}	low	M* (stable)
				intermediate	M* (stable), D* (stable) & unstable points in between
				high	D* (stable)
✓(M), ✗(D)	✓(M), ✗(D)	✗(M,D)	λ_{dyn}^{M}	low	D* (stable)
				intermediate	'sharp' transition
				high	M* (stable)
✗(M), ✓(D)	✗(M), ✓(D)	✗(M,D)	λ_{dyn}^{D}	low	M* (stable)
				intermediate	'sharp' transition
				high	D* (stable)
✓(M,D)	✓(M,D)	✗(M,D)	L_{MT}^{av}	low	D* (stable), M* (stable) & unstable points in between
				intermediate	"
				high	D* (stable)
✓(M), ✗(D)	✓(M), ✗(D)	✓(M), ✗(D)	λ_{dyn}^{M}	low	D* (stable)
				intermediate	stable transition from D to M
				high	M (stable, slightly away from the cell cortex)
✗(M), ✓(D)	✗(M), ✓(D)	✗(M), ✓(D)	λ_{dyn}^{D}	low	M* (stable)
				intermediate	stable transition from M to D
				high	D (stable, slightly away from the cell cortex)
✓(M), ✓(D)	✓(M), ✓(D)	✓(M), ✓(D)	L_{av}^{MT}	low	M (stable)
				intermediate	D(stable), **close to septin ring**
				high	"

to MTs randomly 'grow-and-catch' the KTs, the end possibilities are either amphitelic or syntelic (Fig 3A). In the first scenario, the rapid degradation of wrong attachments resulted in faster attainment of a stable amphitelic configuration (Fig 3B). Thus, in the presence of error correction, all the attachments become amphitelic (Fig 3C, S5 FigA), whereas, in the absence of error correction, half the attachments remain syntelic (Fig 3C). However, both in the presence and absence of error correction, simulations produce almost equal partitioning of chromosomes into mother and daughter cells, i.e., the average fraction of chromosomes in mother relative to daughter cell is ~ 1 (Fig 3D). Clearly, in a population of cells with no error correction in place, the total number of syntelic errors is equally shared by both the SPBs. Hence, statistically, the daughter inherits the same number of chromosomes the mother retains. However, when the error correction is present, the distribution of the fraction of chromosomes in mother relative to daughter is sharp, symmetric having the mean peaked at 0 (in semi-log scale) implying very precise equal chromosome partitioning (Fig 3E). In the absence of error correction, the distribution spreads out (Fig 3E) but still remains symmetric with zero mean (in semi-log scale). The wider distribution, however, characterizes three types of chromosomal partitioning across the divided cell population: (a) mother retains more chromosomes, (b) chromosomes

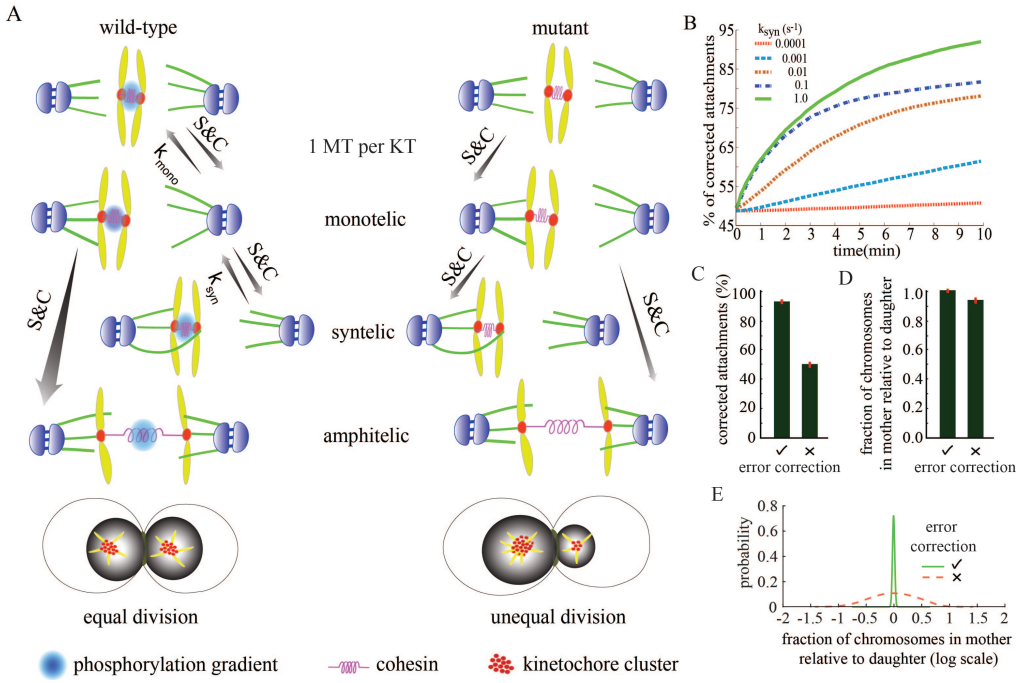

Fig 3. Correction of erroneous attachments and partitioning of chromosomes during division. (A) Schematic depicting possible kinetochore-MT attachments and corresponding chromosomal partitioning patterns. (left panel) Stable amphitelic configurations correlate with equal partitioning of chromosomes in wild-type, whereas (right panel) erroneous attachments (syntelic, monotelic) correlate with unequal partitioning. (B) The dynamics of error correction is correlated with the syntelic degradation rate (k_{syn}). (C) Attachment statistics in the presence (absence) of correction mechanism. ✓/✗ represents the presence/absence of the mechanism. (D) The fraction of chromosomes in the mother relative to the daughter cell in the presence (absence) of the correction mechanism. (E) Representative distributions of the fraction of chromosomes in mother relative to daughter cell in the presence (absence) of error correction mechanism.

are equally shared between mother and daughter, (c) daughter inherits more chromosomes than mother. Statistically, the impaired error correction alone can still produce many equal divisions with single MT-KT attachment.

From this observation, we posit that the accumulation of errors may be necessary, but not a sufficient condition for unequal segregation in *Cryptococcus neoformans*. For the mother to retain more chromosomes on the average, the distribution in absence of error correction (Fig 3E, dotted line) needs to shift toward the right. The fact that the mother retains more chromosomes in Ipl1 depleted cells [17], may relate to the asymmetric functionality of the SPBs, where the properties of nMT nucleation in mSPB differ from that of dSPB [54, 55].

MT nucleation defects and impaired error correction together account for unequal chromosome segregation

Previously, we showed that, upon Ipl1 depletion, the segregated mother-daughter chromosomal volume ratio tends to shift toward > 1, unlike the wild-type scenario where an equal chromosomal division is observed [17]. Note that the segregated chromosomal volume is considered to be proportional to the number of chromosomes. The shift of the ratio toward > 1 upon Ipl1 depletion means that the number of chromosomes is more in the mother compared to the daughter.

To explain the unequal partitioning of chromosomes between the mother and the daughter, we hypothesize that the average number of kinetochore-MT attachments from the SPBs staying in the mother (mSPB) and settling into the daughter (dSPB) may differ. To check that, we explored two plausible scenarios. Firstly, the difference in the number of attachments formed by the mSPB and dSPB may be manifested via a delay in MT nucleation from either of the SPBs. We tested this possibility and our model predicts that a configuration with a greater number of

chromosomes in the mother is feasible when there is a delay in nMT nucleation from the dSPB (Fig 4A). The delay in nMT nucleation from the dSPB enhances the chance of syntelic attachments from the mSPB, associating more chromosomes with the mother.

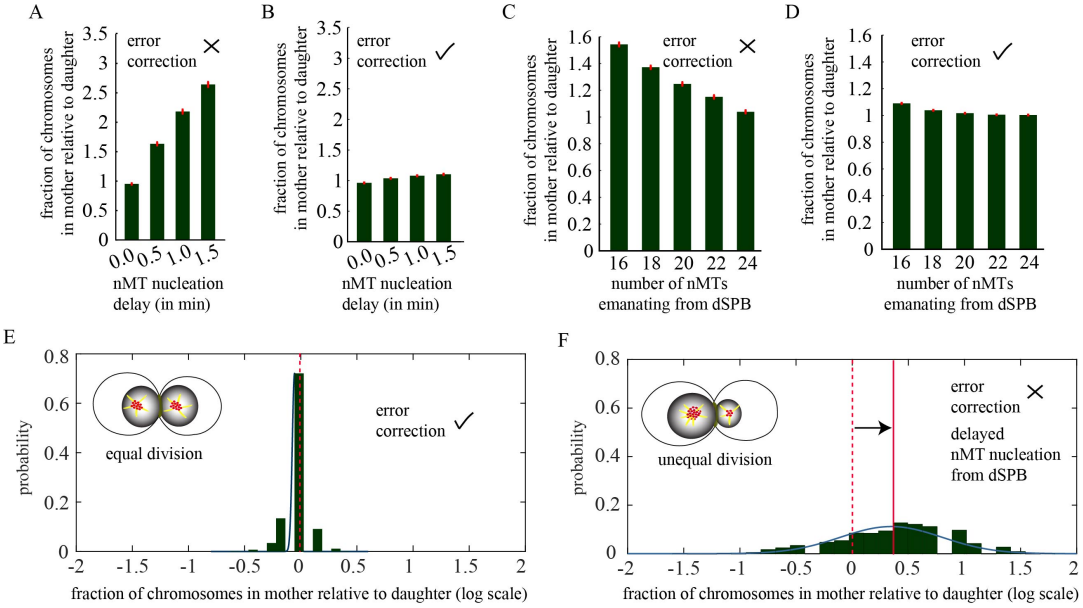

Fig 4. Impaired error correction mechanism together with MT nucleation defects lead to unequal division/aneuploidy. (A-B) Fraction of chromosomes in mother relative to daughter cell as the delay in MT nucleation from dSPB is varied in the absence (A) or presence (B) of error correction. (C-D) Fraction of chromosomes in mother relative to daughter cell as nMT number nucleating from dSPB is varied in the absence (C) or presence (D) of error correction. The number of nMTs from the mSPB is kept constant at 24. (E-F) Distribution of the fraction of chromosomes in mother relative to daughter cell in the wild-type and Ipl1 mutant in semi-log scale.

However, in wild-type cells, since a correction mechanism is present, the initial syntelic attachments made from the mSPB eventually degrade and amphitelic configurations emerge, resulting in an equal partitioning of chromosomes (segregation of the chromosomal volume) (Fig 4B). In Ipl1 depleted cells, since the error correction mechanism is compromised, the syntelic attachments from the mSPB survive. Fig 4A shows that as the MT nucleation from the dSPB delayed, the fraction of chromosomes in the mother relative to daughter cell increases accordingly.

Secondly, we considered that the number of nMTs emanating from the mSPB is greater than that from dSPB. During early spindle assembly, the number of KT-MT attachments from an SPB is proportional to the number of nMTs emanating from the SPB. Thus, it is likely that the mSPB will capture more KTs compared to the dSPB. This also promotes an enhanced number of syntelic attachments from the mother. In the absence of error correction, a comparatively greater number of erroneous attachments from the mSPB are preserved. This leads to the retaining of a greater number of chromosomes by the mother (Fig 4C). However, when the error correction is functional, the syntelic attachments degrade and amphitely is rescued (Fig 4D).

Finally, we tested another possibility where the KTs are captured from multiple MTOCs. In a population of cells with defects in MTOC clustering, it may occur that even after the formation and duplication of the SPBs, some partially clustered MT nucleating fragments are 'left out' (i.e. failed to merge with the SPB). The 'left out' MTOCs may take a long time to fuse with the larger cluster committed to forming the SPBs. If these 'left out' MTOC fragments participate in the KT capture via an MT 'grow-and-catch' mechanism, and later cluster with any of the SPBs, chances of an unequal division becomes prominent in the absence of error correction mechanism (S5 FigB). If 'left out' MTOCs have a greater chance to merge with the mSPB, more chromosomes are kept in the mother compared to the daughter. To conclude, the model predicted distributions of the fraction of chromosomes in both wild type (Fig 4E) and Ipl1 depleted cells, assuming delayed MT nucleation from the dSPB (Fig 4F), appear to correlate with the experimental data in a post-anaphase scenario [17].

Discussion

Our theoretical approach works with a) an agent-based computational model of MT 'grow-and-catch' ('search and capture'), and b) an analytical model to understand the spindle positioning that is partly supported by an agent-based model as well. With the help of the computational model, we examined the role of MT grow-and-catch ('search and capture') in MTOC clustering and partitioning of chromosomes into mother and daughter cells. Using the analytical model, we screen various combinations of the MT-based mechanistic forces and find out plausible mechanical force balance conditions that may orchestrate proper spindle positioning. We reached the following conclusions (Fig 5).

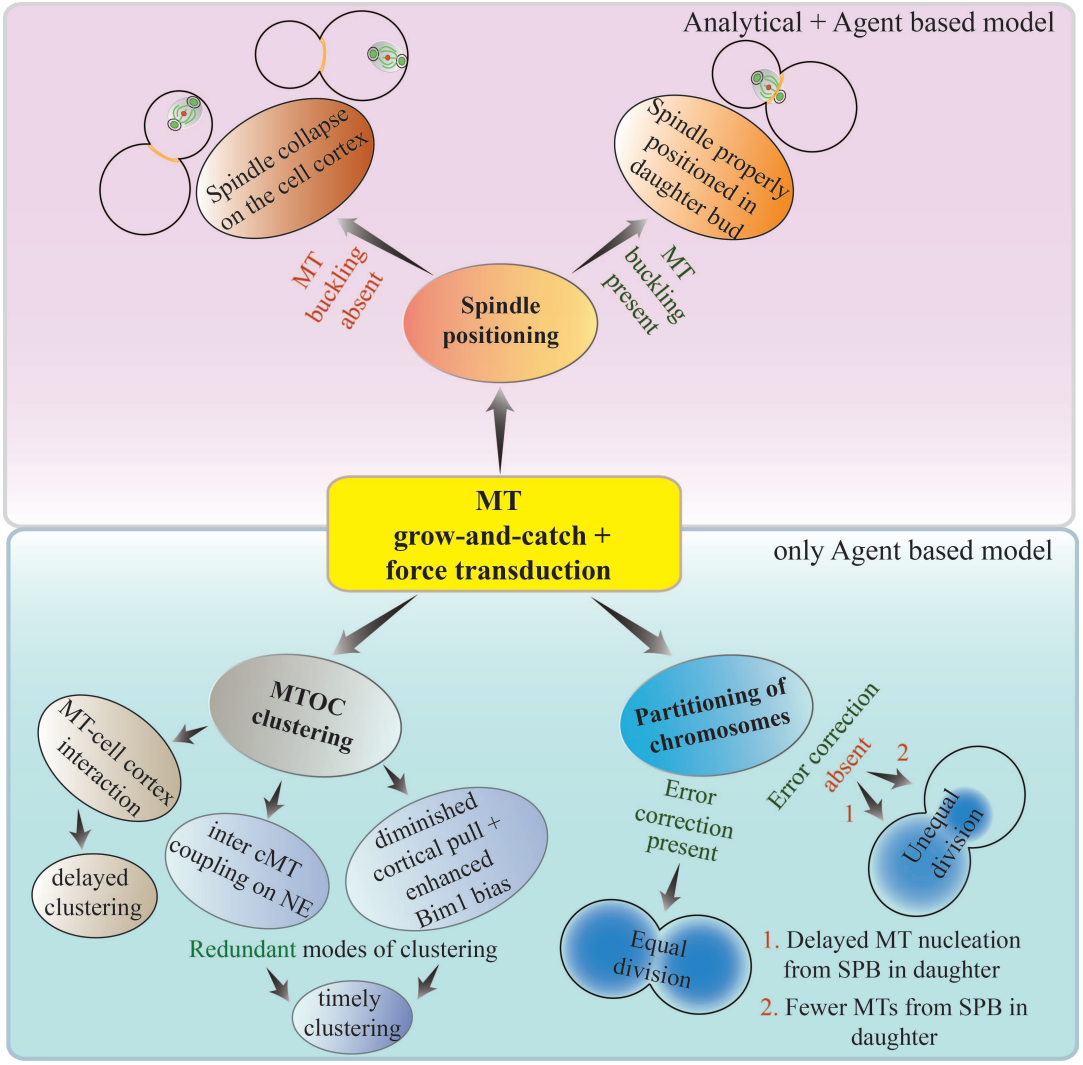

Fig 5. Summary of model outcomes describing mechanistic aspects of MTOC clustering, spindle positioning and chromosomal division in *C. neoformans*. The agent-based model depicts redundant mechanisms for the timely clustering of MTOCs. Inter cMT coupling at NE and/or cortical interaction of MTs with suppressed dynein pull and enhanced Bim1 bias may facilitate timely clustering, either independently or in unison. The agent-based model indicates that impaired error correction alone may not yield much unequal segregation between mother and daughter. The unequal chromosomal division may occur when defects in the error correction mechanism are supplemented by impaired MT nucleation from the SPB in daughter. Furthermore, the analytical model supported by agent-based simulations suggests that proper spindle positioning in the daughter bud near the septin ring requires MT buckling from the cell cortex.

The emergent time scales for MTOC clustering are similar in two scenarios; the design principles of which are based on a) effective inter-MTOC attraction due to minus end-directed motor crosslinking between grazing antiparallel

MTs on the NE and b) effective drift of all the MTOCs towards the septin ring due to Bim1 mediated cortical bias with diminished dynein pull at the cortex. In the first scenario, the clustering time scales down with the minus end motor mediated inward force at the MT-MT overlap. In the latter one, the clustering time scales up with the net cortical dynein pull on the MTs. From a model perspective, the comparable timescales of these two independent clustering mechanisms indicate a possible redundancy between two mechanisms (Fig 1G-1H).

Our analytical model, by screening various MT-based forces, qualitatively highlights the mechanical requirements for proper spindle positioning. It has been suggested that the plane of mitotic division is defined by this stable positioning of the spindle inside the daughter bud with spindle orientation almost parallel to the axis joining the centers of the mother and daughter buds [14, 17, 56]. Our model shows that in the presence of two opposing forces, instantaneous cortical push and dynein pull (no MT buckling), the spindle collapses onto the cortex. Additional force due to MT buckling at the mother and daughter cortex is essential to restore the stable positioning of the spindle near the septin ring. A key reason is the force due to buckling that scales with the inverse square of the MT length. Thus, when the spindle is close to the cortex, buckling MTs strongly push it away preventing the collapse. The analytical model also shows several interesting positions of the spindle which are unstable. The one-dimension model, however, can be extended to higher dimensions which would include several important characteristic degrees of freedom (e.g. orientation of the spindle, the angular displacement of the SPBs, etc.) in the analysis as well.

To examine the physical basis and the consistency of the spindle positioning attributes, the analytical model results are compared with an agent-based computational model. One of the basic differences between the analytical and computational models is the stochastic effects. The computational model entails stochastic fluctuations stemming from the MT dynamic instability, a finite number of MTs, motor activity, etc.; whereas the analytical model, for simplicity, does not contain stochastic fluctuations, as well as temporal degrees of freedom. Possibly, due to intrinsic fluctuations in the computational model, we do not observe any unstable spindle position.

For the timely capture of the chromosomes during spindle assembly, an important factor is the directional bias in the MT searching for KTs. In our simulations, the nMTs explore the nuclear volume and search for KTs clustered within. Since the SPBs remain adjacent immediately after the duplication, all the KTs get uniformly exposed to nMTs from both the SPBs. We consider that nMTs start searching for the KTs ('grow-and-catch'/'search and capture') soon after the SPB duplication and examined various pathways for the KT capture: (a) nMTs from the SPBs grow in random directions searching the entire nuclear volume (S6 FigA), (b) nMT are nucleated toward the KT cluster - accordingly, the nMTs do not explore the whole nuclear volume (S6 FigB), (c) nMTs are prevented from premature catastrophe by the gradient (S6 FigC) or (d) the absolute local concentration of RanGTP-like chemical sensed by the growing MT tip directed toward the KT cluster (S6 FigD). Similar pathways explored in previous studies appeared to be the crucial determinant of the MT driven search process. In fact, in fission yeast, it has been observed that nMTs explore a section of the constrained nuclear volume via pivoted diffusion while searching for the KT [57–59]. Previous computational and experimental studies illustrated the evidence of a similar gradient dependent MT stabilization rendering a higher MT density near the chromosomes [31, 50, 60]. In the present model system, it turns out that over a range of nMT-number, the capture time for all the KTs does not vary significantly across the mechanisms explored in the simulation. One possibility for this outcome could be the proximity of the SPBs and the KTs soon after the duplication.

In general, the KT capture via the MT grow-and-catch process leads to four possible configurations of KT-MT attachments [53, 61]. Once the sister KTs are captured by MTs from opposite SPBs, stable amphitelic attachments are established. When sister KTs are linked to the same SPB, erroneous syntelic attachments are established. If only one sister KT is attached to the pole, monotelic attachments are formed. Another plausible configuration is when both the sister KTs are unattached. Since the model assumes a single MT can attach to a KT, the merotelic error, where at least one sister KT is attached to both the SPBs, does not occur. The erroneous non-amphitelic kinetochore-MT attachments lead to various defects due to unequal segregation; the ramifications of which are attributed to cancer [53, 62, 63]. The amphitelic attachments may be achieved progressively by two central mechanisms. First, the error-correction mechanism that detects and destabilizes the incorrect kinetochore-MT attachments, thereby giving cells a chance to achieve biorientation. Second, the spindle assembly checkpoint (SAC) senses the attachment state of the KTs and delays the anaphase onset until amphitely is achieved. Previous studies report that the error-correction mechanism in budding yeast is governed by the Aurora B kinase homolog Ipl1 where erroneous kinetochore-MT attachments (e.g. low tension syntelic attachments) are degraded via Ipl1 mediated phosphorylation of individual kinetochore proteins. The high-tension bioriented amphitelic attachments stays out of Ipl1 phosphorylation cloud and remain stable [53, 64–68]. In absence of Ipl1-mediated phosphorylation gradient, abundant stable syntelic attachments

are established in Ipl1 depleted cells.

Our model outcome justifies that an impaired error correction mechanism alone may not be responsible for the dominant unequal partitioning of the chromosomes between mother and daughter cells. For unequal segregation, the erroneous attachments must be unequally shared between the mother and the daughter SPBs. This may occur when the MT nucleation/stabilization from either the mother or the daughter SPB is impaired. Earlier experiments in *C. neoformans* [17] show that the mother cell retains more chromosomes compared to the daughter cell upon Ipl1 depletion. Our simulations indicate that impaired MT nucleation from the dSPB may contribute to the accumulation of a greater number of chromosomes in the mother. Several studies refer asymmetric functionality of the SPBs (such as maturation delay between the two SPBs [69–71]) leading to the difference in the MT number [72, 73].

In the current study, we constructed a phenomenology based model that consistently explores various aspects of spindle assembly during mitotic cell division. Using the model, we have been able to elucidate several important features of MTOC clustering, spindle positioning, and chromosomal segregation, largely from a mechanistic point of view (Fig 5). However, the attributes of the dynamic processes involved in the mitotic cell cycle differ widely across different cell types. Different organisms evolved (with increasing complexity at the molecular level) to self-engineer the process of cell division. Thus, investigating the mechanistic principles of the cell division across different organisms using a systems biology-based approach in collaboration with molecular biology experiments stands as the subject of future research.

Materials and methods

Media and growth conditions

The conditional mutant strains harboring the GAL7 promoter were grown in YPG (1 % yeast extract, 2 % peptone, 2 % galactose) as a permissive medium and YPD (1 % yeast extract, 2 % peptone, 2 % dextrose) as a non-permissive medium at 30° C. The wild-type and deletion mutant strains were grown in YPD at 30° C.

Microscopic image acquisition and processing

The conditional mutant strain CNNV104 was grown till OD600=1 in the permissive medium and re-inoculated in the non-permissive media for 8 h to deplete the subcellular protein. The wild-type strains CNVY107 and CNVY177 were grown in YPD and YPG, respectively overnight. The cells were washed once with 1x phosphate-buffered saline (PBS)to form a suspension. The cell suspension was placed on an agarose (2%) patch present on the slide which was covered by a coverslip. The images were acquired at room temperature using laser scanning inverted confocal microscope LSM 880-Airyscan (ZEISS, Plan Apochromat 63x, NA oil 1.4) equipped with highly sensitive photo-detectors or Axio Observer Calibri (ZEISS). The Z- stack images were taken at every 0.5 μm and processed using ZEISS Zen software/ImageJ. All the images were displayed after the maximum intensity projection of images at each time using ImageJ.

Post-acquisition analysis

The budding indices of cells were calculated as the ratio of the diameter of the daughter cell to the diameter of the mother cell. The diameters were measured by drawing a straight line using a line tool in ImageJ.

Simulation Procedure

Modeling the cellular confinement

The geometric construction of the whole cell is considered to be the intersection of two unequal spheres representing the mother bud (radius R_M) and the daughter bud (radius r_D). The septin ring is marked by the circle spanned at the intersection of the two spheres. The mother bud volume remains constant, while the growth rate of the daughter bud is tuned taking a cue from the experimental observations. The nucleus is taken as a sphere (radius r_{nuc}). Underneath the cell boundary, a cortical layer of finite width l_c accounts for the MT interaction at the cortex. The characteristic parameters (e.g. dynein density etc.) of the cortical layer at the mother bud and the daughter bud are controlled independently due to possible functional differences at the molecular level [14, 17].

Table 4. Description of MT based forces present in the *in silico* model

forces	origin	direction
instantaneous push ($F^{cell-mem}_{push-inst}$)	MT tip hitting the cell wall	directed along the MT, away from the cell wall
dynein mediated cortical pull (F^{cor}_{dyn})	MT sliding in cell cortex	directed along the MT, toward the cell cortex
Bim1 bias (F^{cor}_{Bim1})	cortical sliding of MTs toward septin ring	directed toward the septin ring
MT buckling (F^{cor}_{buckle})	MTs impinged on the cell boundary	directed along the MT, away from the cell cortex
inter cMT coupling	overlapping antiparallel MTs grazing the NE	directed along the MT, away from the cell cortex
push due to MT polymerization in cortex ($f^{MT-poly}_{cor}$)	cortical resistance on polymerizing MT tip	directed along the MT, away from the cell cortex
force at ipMT-ipMT overlap (f_{ipMT})	collective activity of kinesin-5 motors at ipMT-ipMT overlap	directed along the MT, leading to the separation of the SPBs
push by growing kMTs (f^{growth}_{push})	kMT tip penetrating into the KT	directed along the MT, away from the KT
pull by shrinking kMTs ($f^{shrinkage}_{pull}$)	separation between kMT tip and KT	directed along the MT, pulling the KT

Modeling the MTs

MTs are modelled as semiflexible polymers characterized by four innate dynamic instability parameters, viz, growth velocity (v_g), shrinkage velocity (v_s), catastrophe frequency (f_c) and rescue frequency (f_r). While probing for an alternative mechanism, f_c of the MTs searching for the KT is modulated by the local concentration/gradient of the RanGTP like chemical. MTs hitting the cortex experience dynein pull, undergo buckling transition when pivoted and apply an instantaneous pushing force on the nucleus. A subpopulation of MTs, graze along the cortex and the NE.

Modeling MTOCs and kinetochores

The KTs and MTOCs are modeled similarly as done in the previous studies [14, 17]. MTOCs are rigid spheres embedded on the NE and the movement of the MTOCs is strictly confined to the NE. SPBs also considered as rigid spheres (radius r_{SPB}) and embedded on the nuclear envelop.

Spherical KTs with a hard-core repulsion ($\vec{f}_{intersection}$) prevent any finite overlap amongst the KTs. The repulsive force is proportional to the instantaneous overlap between two overlapping KTs [17]. Sister KTs remain paired with each other by the cohesin spring until metaphase. A Hookean force, proportional to the inter-KT separation, is introduced amongst the sister KTs to account for the effect of the cohesin spring holding them together [14, 17]. In the computational model, the Hookean force is given by $\vec{f}_{cohesin} = K_{cohesin}\vec{d}_{KT-KT}$, where $K_{cohesin}$ is the spring constant and $|\vec{d}_{KT-KT}|$ is the instantaneous separation between two sister KTs. Relevant model parameters are listed in Table 1. The description of various MT mediated force interactions is discussed in the following sections and summarized in Table 4.

Modeling cMT-cell cortex interaction and the inter cMT coupling at the NE

From the MTOCs and later from the SPBs, the cMTs nucleate in any random direction within the cell, excluding the nucleus. Various force transductions due to cMT-cell cortex interaction in the *in silico* model construction are categorically listed in the following.

1. When a growing cMT reaches to the cortex and hits the cell boundary, the steric cell boundary impedes the MT tip against its growth. We characterize the instantaneous force exerted on the MT tip upon each encounter with the

cell boundary as an instantaneous push ($\vec{f}^{cell-mem}_{push-inst}$). The magnitude of the instantaneous push is taken to be 1 pN per MT on each encounter. The net instantaneous push is $\vec{F}^{cell-mem}_{push-inst}=\sum_{cMTs}\vec{f}^{cell-mem}_{push-inst}$.
2. Apart from the instantaneous push, a MT growing inside the cell cortex undergoes sliding. The 'bent' sliding segment inside the cell cortex provides anchorage points for the cortical dyneins. For computational simplicity, we introduce the parameter, mean number of dyneins per unit length in mother (daughter) cortex ($\lambda^{M(D)}_{dyn}$) on the MT segments inside the cortex. The force due to the dynein pull on a cMT ($\vec{f}^{cor}_{dyn}$) is proportional to $\lambda^{M(D)}_{dyn}l_{cor}$, where l_{cor} is the combined length of the penetrated MT segment inside the cell cortex. M, D in the suffix denotes mother and daughter cell cortex respectively. The net cortical dynein pull is $\vec{F}^{cor}_{dyn}=\sum_{cMTs}\vec{f}^{cor}_{dyn}=\sum_{cMTs}\lambda^{M(D)}_{dyn}l_{cor}\ \vec{f}_{dyn}$, where $\vec{f}_{dyn}$ is the force generated by a single dynein motor.
3. Similarly, the force due to Bim1 bias on a cMT within mother cortex is $\vec{F}^{cor}_{Bim1}=\sum_{cMTs}\vec{f}^{cor}_{Bim1}=\sum_{cMTs}\lambda^{M}_{Bim1}l_{cor}$ $\vec{f}_{Bim1}$ where $\vec{f}_{Bim1}$ is the force generated by a single Bim1 motor. The force due to Bim1 is directed toward the septin ring (Table 4). In the daughter cortex, there is no Bim1 bias. For simplicity, we chose $\lambda^{M}_{Bim1}=\lambda^{M}_{dyn}$.
4. The MTs impinged at the cell membrane also undergo buckling transition (we considered first-order Euler buckling in the present context). Whether a MT hitting the cell membrane, deep inside the cortex, will transduce dynein mediated pull or a net push away from the cortex due to Euler buckling or undergo catastrophe is dictated by predefined probabilities $P^{cell-mem}_{buckle}$, $P^{cell-mem}_{dyn-pull}$ and $P^{cell-mem}_{cat}$, where $P^{cell-mem}_{buckle}$ = 1- $P^{cell-mem}_{dyn-pull}$-$P^{cell-mem}_{cat}$. The buckling force ($\vec{f}^{cor}_{buckle}$) is proportional to l^{-2} where l is the concerned cMT length. The net buckling force is $\vec{F}^{cor}_{buckle}=\sum_{cMTs}\vec{f}^{cor}_{buckle}$ ($|\vec{f}^{cor}_{buckle}|=Dl^{-2}$, where D refers to the flexural rigidity of the MT $\sim$ 200 pN μm^2). In mother cortex, $P^{cell-mem}_{dyn-pull}$=0.0, $P^{cell-mem}_{buckle}$=0.5, $P^{cell-mem}_{cat}$=0.5; in daughter cortex, $P^{cell-mem}_{dyn-pull}$=0.8, $P^{cell-mem}_{buckle}$=0.1, $P^{cell-mem}_{cat}$=0.1.
5. Moreover, a polymerizing MT at the cortex experiences resistance from the cortex on the MT tip in the vicinity of the cell membrane. The force exerted on the MT tip due to this resistance is chosen to be Hookean spring-like. We estimate the force on a polymerizing MT ($f^{MT-poly}_{cor}$) deep inside the cortex as $k_{cor}l_{cor}$. Here, k_{cor} is the equivalent spring constant characterizing $f^{MT-poly}_{cor}$ that pushes the MT tip away from the cortex. We evaluate the net push on the MTOCs/SPBs due to MT polymerization inside the cortex ($F^{MT-poly}_{cor}$) by summing the force contributions ($f^{MT-poly}_{cor}$) overall growing MTs within the cortical region ($F^{MT-poly}_{cor}=\sum^{cortex}_{MTs}f^{MT-poly}_{cor}$).

The overall load on a cMT at the cortex due to the resistance from the cortical substance modulates the dynamic instability parameters of the cMT. The intrinsic parameters v_g and f_c are tuned as described in the following: (a) $v_g = v_{g0}\exp(f_{load}/f_{stall})$, where v_{g0} represents the unimpeded growth velocity with no load exerted on the cMT, f_{load} and f_{stall} denote load force and stall force per cMT respectively; (b) $f_c=f^{stall}_c/[1+\ (f^{stall}_c/f_{c0}$ -1) $\exp(f_{load}/f_{stall})]$. The load force $f_{load}\sim -k_{cor}l_{cor}$ [14,17].

To estimate the force due to the inter cMT coupling at the NE $\vec{f}_{overlap}$, we evaluate the net overlap length (l_{ovl}) between a pair of overlapping antiparallel MTs. The force exerted on the MTOCs is proportional to $\lambda_{ovl}l_{ovl}$, where λ_{ovl} is the mean number of minus end-directed motors per unit length at the MT-MT overlap on the NE.

Modeling nMT-kinetochore interaction

The nMTs are categorized into two distinct subsets, interdigitated MTs within the nuclear volume facilitating biorientation of SPBs via molecular motors i.e. interpolar MTs (ipMTs) and MTs establishing contact between SPBs and KTs i.e. kinetochore MTs (kMTs). The collective activity of crossbridging kinesin-5 motors at the ipMT-ipMT overlaps generates a force $f_{ipMT} = l^{ipMT}_{ovl}\lambda_{ipMT}f_{kinesin-5}$ where l^{ipMT}_{ovl} is the total overlapping length summed over all ipMTs emanating from two SPBs. λ_{ipMT} is the average number of kinesin-5 motors per unit length at the ipMT-ipMT overlap. $f_{kinesin-5}$ is the force exerted by a single kinesin-5 motor.

Stochastic growth and shrinkage of the kMTs due to dynamic instability leads to a tug of war between several oppositely directed competing forces. During the growth phase of the kMT, the kMT tip imparts a net push $f^{growth}_{push} = l_{pen}K_{fibril}$ on the KT attached to it. Here, l_{pen} is penetration length of the kMT into the KT, K_{fibril} is the stiffness constant of the connecting spring that mimics the KT fibril in the model. A kMT in shrinkage phase, pulls the KT with a force $f^{shrinkage}_{pull} = l_{separation}K_c$, where $l_{separation}$ is the distance between the kMT tip and the corresponding KT. K_c denotes the stiffness constant of the Hookean spring linking the depolymerizing kMT tip and the KT.

To maintain a constant gap between the SPBs and the KT cluster, a length-dependent catastrophe of the kMTs has been incorporated in the model. The catastrophe frequency of a kMT (f_c) is regulated in the following manner, $f_c = hl_{kMT}$, where l_{kMT} is the kMT length [14,17].

Equations of motions governing the spatiotemporal dynamics of the nucleus, MTOCs, kinetochores, SPBs

Forces due to single cMT interacting with the cortex, are applied on the nucleus and the MTOCs/SPBs, simultaneously. Additionally, the force stemming from the ipMT interaction is also exerted on the SPBs. If $\vec{F}_{nucleus}$, $\vec{F}_{MTOC}$ and $\vec{F}_{SPB}$ are the net resultant forces exerted on the nucleus, MTOC and SPB respectively, the corresponding equations of motion can be gleaned as,

$$\frac{d\vec{R}_{nucleus}}{dt} = \frac{\vec{F}_{nucleus}}{\zeta_{nucleus}} \tag{1}$$

$$\frac{d\vec{R}_{MTOC}}{dt} = \frac{\vec{F}_{MTOC}}{\zeta_{MTOC}} \tag{2}$$

$$\frac{d\vec{R}_{SPB}}{dt} = \frac{\vec{F}_{SPB}}{\zeta_{SPB}} \tag{3}$$

where $\vec{R}_{nucleus}$, $\vec{R}_{MTOC}$ and $\vec{R}_{SPB}$ denote the instantaneous positions of the nucleus, MTOCs and SPBs respectively, at a certain time step. $\zeta_{nucleus}$, ζ_{MTOC}, ζ_{SPB} represent viscous drag on the corresponding objects. $\vec{F}_{nucleus}$, $\vec{F}_{MTOC}$ and $\vec{F}_{SPB}$ contain vectorial contributions from $\vec{F}_{cor}^{MT-poly}$, $\vec{F}_{push-inst}^{cell-mem}$, $\vec{F}_{dyn}^{cor}$ and $\vec{F}_{buckle}^{cor}$.

In a similar fashion, the motion of a KT is dictated by the following equation of motion,

$$\frac{d\vec{R}_{kinetochore}}{dt} = \frac{\vec{F}_{kinetochore}}{\zeta_{kinetochore}} \tag{4}$$

Here, $\vec{R}_{kinetochore}$, $\vec{F}_{kinetochore}$ and $\vec{\zeta}_{kinetochore}$ represent instantaneous position, net force on the KT and the viscous drag experienced by the KT respectively. $\vec{F}_{kinetochore}$ entails a vectorial summation over $\vec{f}_{push}^{growth}$, $\vec{f}_{pull}^{shrinkage}$, $\vec{f}_{ipMT}$, $\vec{f}_{cohesin}$ and $\vec{f}_{intersection}$. For simplicity, we have not considered contributions of thermal diffusion (Brownian motion) while computing the positional update of any of the objects considered in the model.

The equations of motion are discretized and solved using Euler's method at every time step.

Mathematical model for spindle positioning in budding yeast

In 2-dimensions we consider that the mother and the daughter bud constitute two intersecting circles of radii R_M and r_D respectively. The axis of symmetry of the cellular confinement (e.g. the mother-daughter conglomerate) is taken to be the X-axis with the origin 'O' at the center of the mother bud. The center of the daughter bud is placed at a distance 'd' from the center of the mother (Fig S2 FigA). We compute various MT-based forces on the spindle upon MT interaction with the cell cortex. The mathematical formulation of various force balance terms (e.g. forces originating from MT pushing, dynein mediated pull on the MTs at the cell cortex, MT buckling, etc.) is characterized by exponential length distribution of MTs [23, 35]. The direction of the forces is depicted in Fig S2 FigB.

Pushing forces

MTs are nucleated from the two SPBs separated by a distance of $2a$ (spindle length) with spindle-center at x. For convenience, we mark the SPB located at the left of the spindle ($SPB(L)$) and the SPB located at the right of the spindle ($SPB(R)$). When an MT nucleates out of the $SPB(L)$, it grows a distance $R_M + x - a$ to establish contact with the cell membrane (S2 FigA). Hence, the instantaneous pushing force on the $SPB(L)$ due to the microtubules hitting the mother cell membrane reads,

$$F_{push-inst}^{cell-mem(M)} = A_M e^{-(R_M+x-a)/L_{MT}^{av}} \tag{5}$$

The exponential weight factor enters the expression due to the length of dynamic MTs governed by the following distribution: $N(l) \propto e^{-l/L_{MT}^{av}}$ where l is the length of the MT under consideration. The instantaneous pushing force from the MTs nucleating out of the $SPB(R)$ has to elongate up to a distance $d + r_D - x - a$ along the axis of

symmetry to make a contact with the cell membrane in the daughter bud. Hence, the instantaneous pushing force contribution from the daughter bud cell membrane is,

$$F_{push-inst}^{cell-mem(D)} = A_D e^{-(d+r_D-x-a)/L_{MT}^{av}} \tag{6}$$

Here A_M and A_D define the amplitude of the instantaneous pushing force contribution from the mother and the daughter cell membrane. The prefactors A_M and A_D are proportional to the number of MTs interacting with the cell membrane where instantaneous pushing force per MT is taken to be ~ 1 pN.

Pulling forces

When a MT emanating from the $SPB(L)$ grows all the way to penetrate the mother cortex, the dyneins localized at the cortex anchor to the MT segment orchestrating a net pull ($F_{dyn}^{cor(M)}$) toward the mother cortex. Since an elongating MT segment inside the cortex can bend and undergoes sliding as illustrated in the schematic diagram, the pulling force is categorized into two parts: 1. the pull on the uncurled/straight MT segment in the cortex and 2. the pull on the MT segment engaged in 'lateral sliding' along the cortex. Similarly, MTs nucleating out of the $SPB(R)$ upon elongating up to the daughter cortex can penetrate and experience dynein mediated pull. For a MT nucleating from the $SPB(L)$ within the one-dimensional confinement, it has to extend at least up to a distance of $R_M - l_c + x - a$ to establish a physical contact with the mother cortex. It is also evident from the schematic diagram that after reaching the cortex the 'uncurled' MT tip can advance up to $R_M + x - a$ without bending (S2 Fig). Henceforth the net pull on the $SPB(L)$ from the 'uncurled' MT segments in the mother cortex can be evaluated in the following manner.

$$\begin{aligned} F_{dyn(uncurled)}^{cor(M)} &= B_M \lambda_{dyn}^M \int_{R_M-l_c+x-a}^{R_M+x-a} e^{-(s+x-a)/L_{MT}^{av}} ds \\ &= B_M \lambda_{dyn}^M L_{MT}^{av} (e^{l_c/L_{MT}^{av}} - 1) e^{-(R_M+2x-2a)/L_{MT}^{av}} \end{aligned} \tag{7}$$

In a similar manner, we can also evaluate the net dynein pull contribution from the 'arc' like MT segment sliding within the mother cortex. Therefore, the net force due to the dynein pull on the sliding 'arc' $F_{dyn(sliding)}^{cor(M)}$ reads

$$\begin{aligned} F_{dyn(sliding)}^{cor(M)} &= B_M \lambda_{dyn}^M \int_0^{l_{arc}^M} ds\ e^{-(R_M+x-a+s)/L_{MT}^{av}} \\ &= B_M \lambda_{dyn}^M L_{MT}^{av} e^{-(R_M+x-a)/L_{MT}^{av}} (1 - e^{-l_{arc}^M/L_{MT}^{av}}) \end{aligned} \tag{8}$$

Here l_{arc}^M is the 'arc' like segment traced from the intersection of the axis of symmetry and the mother cell membrane to the peripheral contact of the septin ring with the mother cell membrane. Here for the sake of simplicity, we assume that the sliding MTs passing through the mother cortex extend up to the septin ring. The value of l_{arc}^M is estimated to be

$$l_{arc}^M = \frac{\pi R_M}{2} + R_M \tan^{-1}(x_{sp}/y_{sp}) \tag{9}$$

From $SPB(R)$ we assume that the MTs nucleate in the direction of the daughter bud and interact with the daughter cortex and orchestrate a pull ($F_{dyn}^{cor(D)}$) in a similar fashion with which MTs from $SPB(L)$ interact with the mother cortex. Thus, the net pull due to the anchored dyneins on the 'uncurled' MT segments inside the daughter cortex reads,

$$\begin{aligned} F_{dyn(uncurled)}^{cor(D)} &= B_D \lambda_{dyn}^D \int_{d+r_D-l_c-(x+a)}^{d+r_D-(x+a)} ds\ e^{-(d+s-x-a)/L_{MT}^{av}} \\ &= B_D \lambda_{dyn}^D L_{MT}^{av} (e^{l_c/L_{MT}^{av}} - 1) e^{-(2d-2x-2a+r_D)/L_{MT}^{av}} \end{aligned} \tag{10}$$

Similarly, we can compute the contribution in the net dynein pull on $SPB(R)$ from the 'sliding arc' passing through the daughter cortex in the following manner.

$$\begin{aligned} F_{dyn(sliding)}^{cor(D)} &= B_D \lambda_{dyn}^D \int_0^{l_{arc}^D} ds\ e^{-(d+r_D-x-a+s)/L_{MT}^{av}} \\ &= B_D \lambda_{dyn}^D L_{MT}^{av} e^{-(d+r_D-x-a)/L_{MT}^{av}} (1 - e^{-l_{arc}^D/L_{MT}^{av}}) \end{aligned} \tag{11}$$

Here, l^D_{arc} is estimated to be the arc length traced from the intersection of the axis of symmetry with the daughter cortex and the peripheral contact of the septin ring with the cell membrane. From the schematic diagram we obtain the l^D_{arc} to be

$$l^D_{arc} = \frac{\pi r_D}{2} + r_D \tan^{-1}\left(\frac{d - x_{sp}}{y_{sp}}\right) \tag{12}$$

Note here that the prefactors B_M and B_D are proportional to the number of MTs experiencing dynein mediated pulling in the mother and the daughter cortex respectively.

In the above analysis, we have assumed that the effective dynein density is smeared uniformly across the whole mother and daughter cortex. However, experimental observations point toward a non-uniform, differential spatial arrangement of dyneins in the mother and the daughter cortex. These observations prompted us to accommodate the differential spatial profiling of dynein in the mother and the daughter cortex into the current mathematical model. Force transduction due to the differential spatial organization of dyneins in the mother and daughter cortex is described in detail in the S1 Text.

Buckling forces

MTs with tips passed into the mother(daughter) cortex can buckle where the buckling probability is a tunable parameter in the current model. MTs impinged and pivoting at the mother(daughter) cortex generate a length-dependent 'pushing' force that increases with the squared inverse length of the MT while undergoing buckling. It is evident from the geometric construction that the forces stemming from MT buckling at the mother and daughter cortex are oppositely directed (S2 Fig). We have taken the following form for the force produced by cortical buckling at the mother cortex ($F^{cor(M)}_{buckle}$)

$$F^{cor(M)}_{buckle} = -\frac{D_M}{(R_M + x - a)^2}\, e^{-(R_M + x - a)/L^{av}_{MT}} \tag{13}$$

Similarly, force generated due to the buckling at the daughter cortex $F^{cor(D)}_{buckle}$ is taken as

$$F^{cor(D)}_{buckle} = -\frac{D_D}{(d + r_D - x - a)^2}\, e^{-(d + r_D - x - a)/L^{av}_{MT}} \tag{14}$$

D_M and D_D are the average number of MTs undergoing buckling transition in the mother and daughter cortices, respectively.

Supporting information

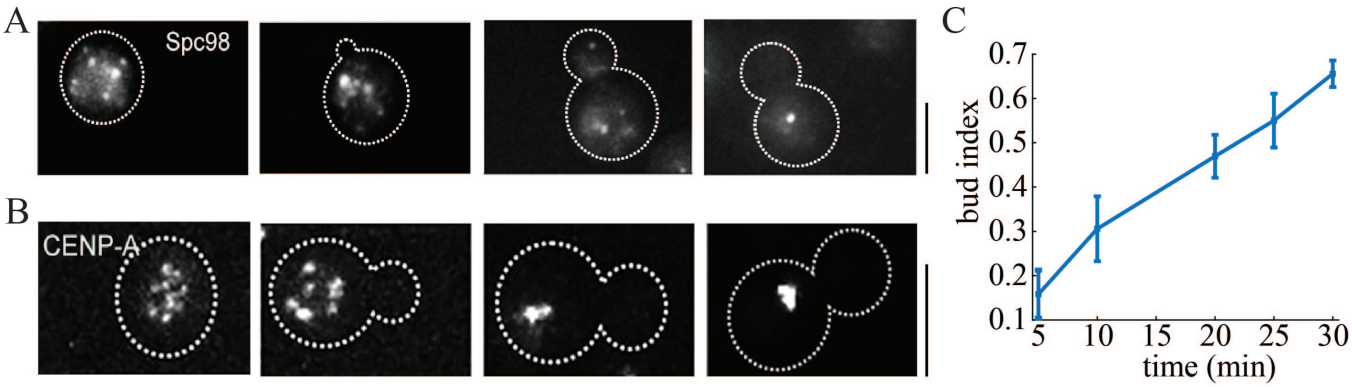

S1 Fig. Clustering of MTOCs and KTs during mitosis. Images of cells showing the localization of (A) Spindle pole body protein, Spc98 and (B) KT marker CENP-A at different stages of the cell cycle in the wild-type cells. Bar, 5 μm. (C) Progression of bud growth with time.

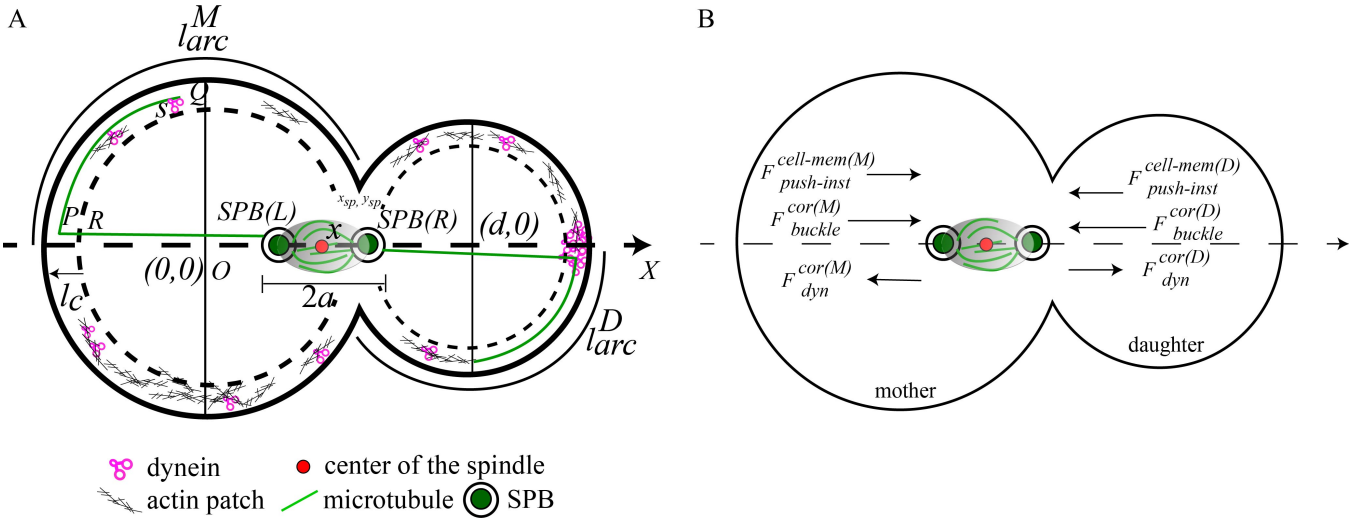

S2 Fig. Schematic diagram depicting the one-dimensional mathematical model for spindle positioning. (A) In the model the origin $O(0,0)$ is located at the center of the mother bud while the center of the daughter bud is located on the axis of symmetry for the geometric confinement under consideration (namely the X axis) at $(d,0)$. The radii of the mother bud and the daughter bud are R_M and r_D respectively. The instantaneous position of the spindle is denoted by x measured from the origin. The +ve X axis extends from the mother to the daughter bud. The width of both the mother and the daughter cortex is taken as l_c. The black 'mesh-like' patches at the peripheral cortical region of the mother and the daughter bud represent actin network with dyneins marked structures in white-magenta. $SPB(L)$ and $SPB(R)$ denote the leftward and rightward SPBs and the green lines represent microtubules. In the mother bud, the section 'RP' is the 'uncurled' MT segment in the cortical region and the segment 'PQ' denotes the 'curled' MT segment undergoing sliding within the mother cortex. Cortical dyneins interact with both the segments and give rise to the dynein mediated pull. A similar structural template applies to the daughter cortex as well. Localized cortical dynein patch in the daughter cortex around the axis of symmetry signifies the differential spatial distribution of dynein in the mother and daughter bud. (B) The direction of the forces acting on the spindle.

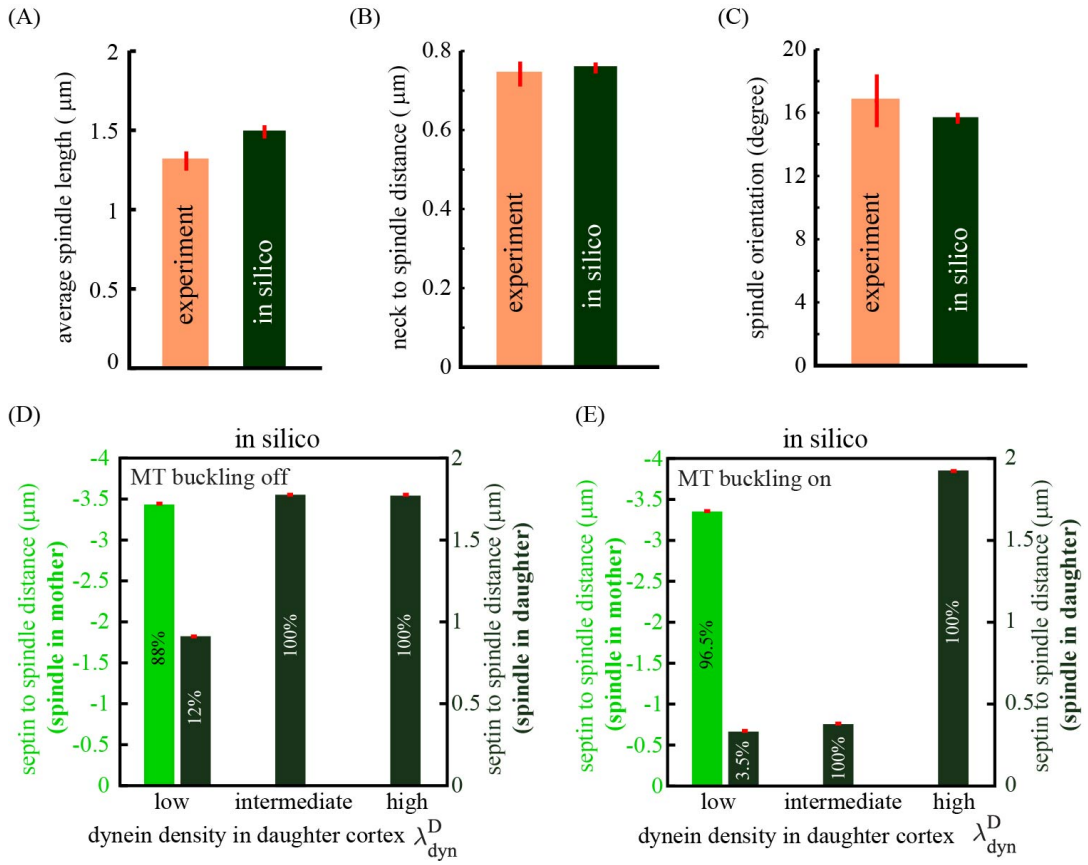

S3 Fig. Multiple characteristics of spindle architecture and localization. (A) The length of the spindle (n=68, experiment) in metaphase cells is shown. (B) The spindle to neck (junction of mother-daughter bud) distance in the wild-type (n=70, experiment). (C) The spindle orientation with respect to the mother-daughter axis (n=52, experiment). (D-E) Spindle distance from septin ring in the absence (D) or presence (E) of MT buckling at the cortex. The values within the bars indicate the percentage of spindles in mother or daughter, across the cell population. +ve/-ve sign in distance indicates the spindle position inside the daughter/mother bud. In all figures, n > 2000 for simulation and red bars indicate SEM (wherever shown).

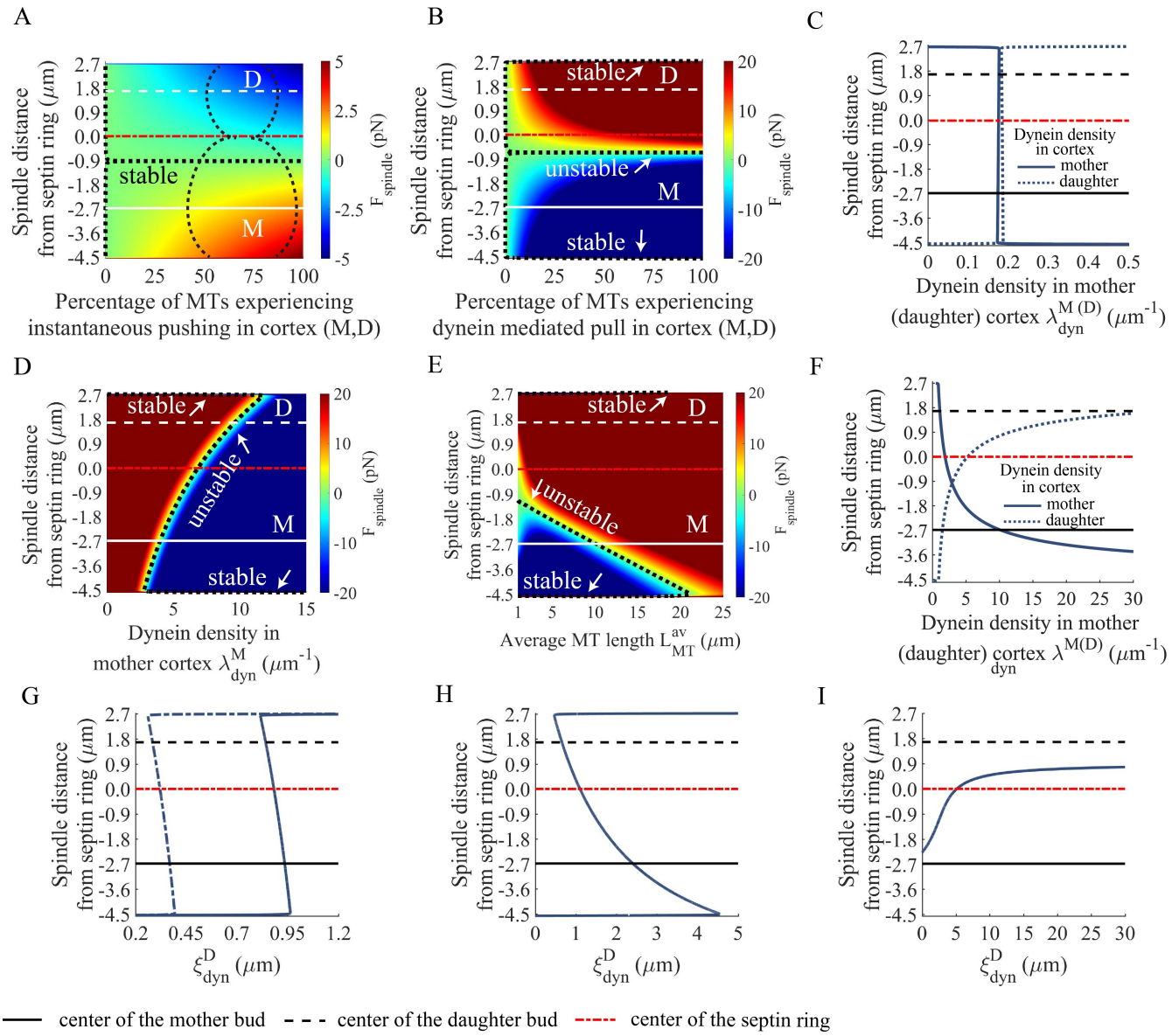

S4 Fig. Effect of various force combinations on spindle positioning. In all figures, -ve/+ve distance refers to the spindle in mother (M)/daughter (D) bud. In the color maps, white dashed and solid lines denote the center of the daughter and mother bud respectively; color bars represent net force on the spindle. (A) In presence of instantaneous cortical push from the mother and daughter cortex, the spindle stabilizes (dotted black line) close to the septin ring inside the mother bud. (B) In presence of dynein mediated cortical pull from the mother and daughter cortex, the spindle collapses onto the cell cortex. An unstable spindle position is found in between. (C) Variation in dynein pull from mother (daughter) cortex ($\lambda_{dyn}^{M(D)}$) with instantaneous cortical push from mother (daughter) cortex acting alongside. The spindle collapses either onto the mother cortex or onto the daughter cortex. (D) Spindle position upon variation in dynein density in the mother cortex (λ_{dyn}^{M}) with fixed dynein density in the daughter cortex. Instantaneous cortical push is present in both mother and daughter. (E) Spindle position upon variation in average MT length (L_{MT}^{av}) when instantaneous cortical push and dynein pull are combined. (F) Spindle position upon variation in dynein density in mother (daughter) cortex ($\lambda_{dyn}^{M(D)}$) when instantaneous push, dynein pull, and MT buckling in mother (daughter) cortex act together. MT buckling force (directed away from cortex) dominates close to the mother (daughter) cortex. (G) Variation of the characteristic length scale spanning the localized dynein

patch in the daughter cortex (ξ^D_{dyn}) yields unstable spindle positions slotted in between stable fixed positions of the spindle position in the mother and the daughter cortex while mutually opposing MT mediated instantaneous push and dynein pull solely from the daughter cortex compete against each other. For this particular scenario, force transduction from the mother cortex is switched 'off'. Relevant parameters: $\lambda^D_{dyn} = 1\ \mu\text{m}^{-1}$ (solid line) and $2\ \mu\text{m}^{-1}$ (dashed line), $A_D = 5$ pN. (H) Variation in the characteristic length scale accounting for the size of localized dynein patches in the daughter cortex (ξ^D_{dyn}) results in unstable fixed positions as the spindle undergoes a gradual spatial transition from the stable fixed positions at the mother cortex to the stable fixed positions at the daughter cortex. The force balance landscape is governed by cortical pull stemming from the mother and daughter cortex only (relevant parameters: λ^M_{dyn} =1 μm^{-1}; $\lambda^D_{dyn} = 4.5\ \mu\text{m}^{-1}$). (I) In presence of MT buckling transition together with instantaneous push and dynein pull from the mother and the daughter cortex, stepwise increment in ξ^D_{dyn} enhances net pull toward the daughter resulting in a stable spindle positioning inside the daughter bud.

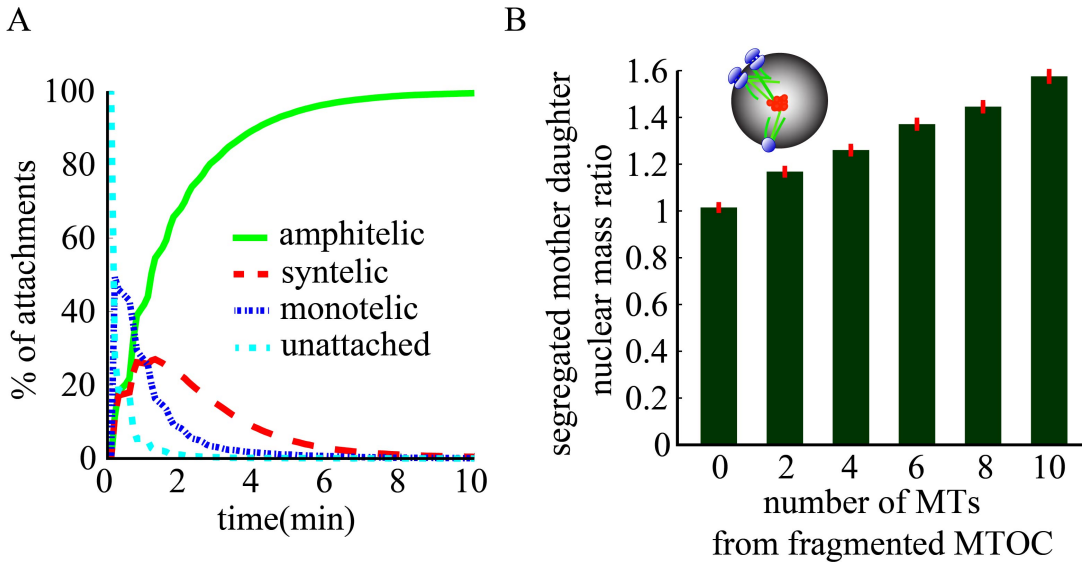

S5 Fig. Additional numerical tests for error correction and chromosomal partitioning. (A) At the onset of KT capture by MT 'grow-and-catch' mechanism, *de novo* stabilization of amphitelic attachments and degradation of erroneous attachments progressively lead to a ploidy statistics within ~ 10 min of 'grow-and-catch' having syn(mono)-telic degradation rate k_{syn} (k_{mono})=1/min. (B) As a consequence of impaired MTOC clustering, just after the delayed SPB maturation and duplication apart from the duplicated SPBs, there is a possibility of having a partially clustered fragmented MTOC embedded on the NE. In a structural template where the MTs from the 'left out' MTOC fragment also participate in KT capture, and later the 'left out' MTOC merges with any of the two matured SPBs, unequal segregation emerges. Further, as a model constraint, if the condition that the fragment fuses with the SPB of the mother bud is imposed, a higher amount of chromosomal volume would be shared by the mother bud. As the number of MTs from the MTOC fragment is increased, the ratio tends to shift toward a higher value > 1 in absence of error correction mechanism.

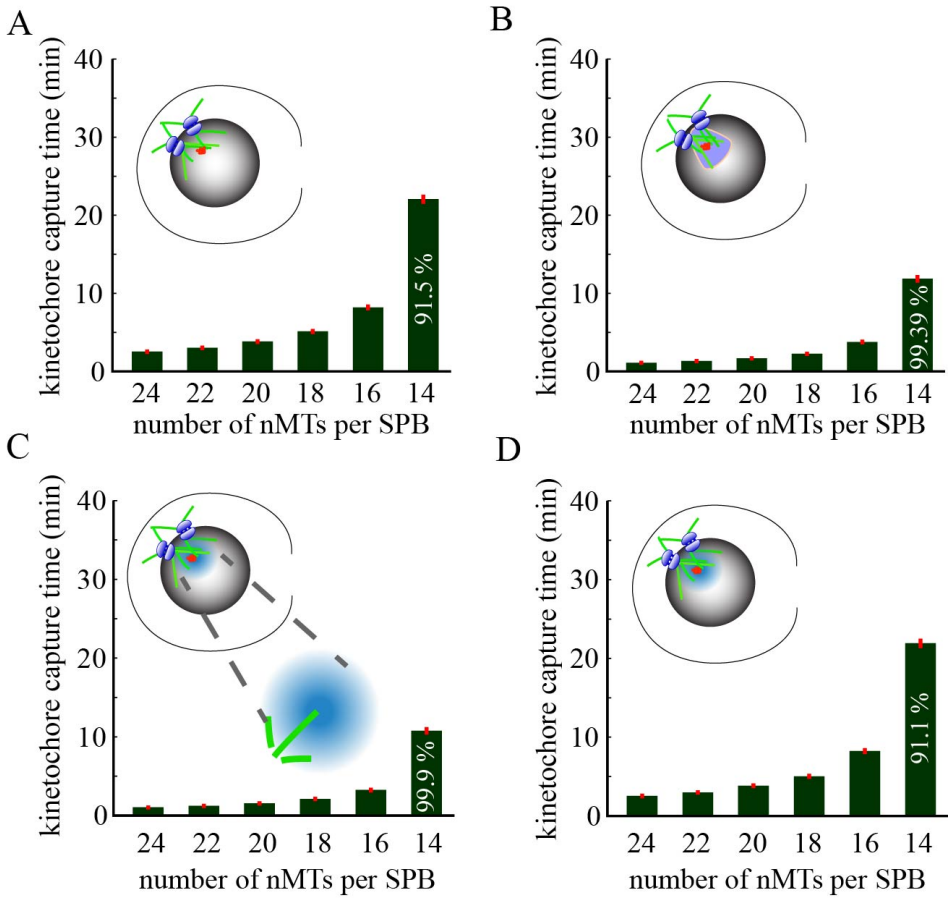

S6 Fig. KT capture by 'searcher' microtubules. The KT cluster is located halfway in between the SPBs and the center of the nucleus (A) KT capture time when nMTs explore the nuclear volume isotropically. (B) KT capture time when the nMT nucleation is biased toward the KT cluster marked by the purple cloud/envelope in the inset schematics. (C) KT capture-time when the direction of MT growth is modulated by the local concentration gradient similar to RanGTP. Higher the concentration gradient around the nMT plus end, lower the chance of undergoing catastrophe. (D) KT capture-time when the direction of MT growth is modulated by the local absolute concentration of the chemical cue that stabilizes nMTs undergoing premature catastrophe. Higher the chemical concentration around the nMT plus end, lower the chance catastrophe.

S1 Text. MTOC clustering and chromosomal division through proper spindle positioning in yeast: a microtubule grow-and-catch model. This file comprises the following sections: 1. *One-dimensional mathematical model describing the forces due to localized dynein organization in the daughter cell cortex.* This section describes the mathematical calculation of estimating cortical pull when spatial organization of dyneins is localized. 2. *Model assumptions.* This section discusses about the assumptions considered in the analytical model of spindle positioning. 3. *Additional numerical analysis of the analytical model.* This section explores the combinatory effects of various MT mediated forces on proper spindle positioning. (PDF)

S1 Video. MTOC clustering facilitated via inter-cMT coupling at the Nuclear Envelop (NE). MTOCs are blue; KTs are magenta; MTs are green.

S2 Video. MTOC clustering facilitated via MT-cell cortex interaction. Force produced by single dynein on each MT at mother cortex ($|\vec{f}_{dyn}|$) is chosen to be 1.0 pN. Bias force towards septin ring produced by single Bim1 on each MT at mother cortex ($|\vec{f}_{Bim1}|$) is chosen to be 0.0 pN. MTOCs are blue; KTs are magenta; MTs are green.

S3 Video. MTOC clustering facilitated via MT-cell cortex interaction (enhanced Bim1 bias + suppressed dynein activity). Force produced by single dynein on each MT at mother cortex ($|\vec{f}_{dyn}|$) is chosen to be 0.0 pN. Bias force towards septin ring produced by single Bim1 on each MT at mother cortex ($|\vec{f}_{Bim1}|$) is chosen to be 1.0 pN. MTOCs are blue; KTs are magenta; MTs are green.

Acknowledgments

This work was supported by the fellowship from SERB (Science and Engineering Research Board), Department of Science and Technology (DST), India (EMR/2017/001346) to RP and Tata Innovation Fellowship (BT/HRD/35/01/03/2017) to KS. SC was supported by fellowship from the University Grants Commission (UGC), India, SS was supported by the fellowship from INSPIRE (IF131156) program DST, India, and NV was supported by the fellowships (09/733 (0253)/219-EMR-I) and 9/733 (0161)/2011-EMR-I from Council of Scientific & Industrial Research (CSIR), India.

References

1. Dogterom M, Leibler S. Physical Aspects of the Growth and Regulation of Microtubule Structures. Physical Review Letters. 1993;70(9):1347–1350.
2. Wu J, Akhmanova A. Microtubule-Organizing Centers. Annu Rev Cell Dev Biol. 2017;33:4.1–4.25.
3. Bornens M. The centrosome in cells and organisms. Science. 2012;335:422–26.
4. Conduit PT, Wainman A, Raff JW. Centrosome function and assembly in animal cells. Nat Rev Mol Cell Biol. 2015;16:611–24.
5. Rodionov V, Nadezhdina E, Borisy G. Centrosomal control of microtubule dynamics. PNAS. 1999;96:115–20.
6. Chabin-Brion K, Marceiller J, Perez F, Settegrana C, Drechou A, Durand G, et al. The Golgi complex is a microtubule-organizing organelle. Mol Biol Cell. 2001;12:2047–60.
7. Hurtado L, Caballero C, Gavilan MP, Cardenas J, Bornens M, Rios RM. Disconnecting the Golgi ribbon from the centrosome prevents directional cell migration and ciliogenesis. Journal of Cell Biology. 2011;193:917–33.
8. Vinogradova T, Paul R, Grimaldi AD, Loncarek J, Miller PM, Yampolsky D, et al. Concerted effort of centrosomal and Golgi-derived microtubules is required for proper Golgi complex assembly but not for maintenance. Mol Biol Cell. 2012;23:820–33.
9. Vinogradova T, Miller PM, Kaverina I. Microtubule network asymmetry in motile cells: role of Golgi-derived array. Cell Cycle. 2009;8:2168–74.
10. Paz J, Lüders J. Microtubule-Organizing Centers: Towards a Minimal Parts List. Trends in Cell Biology. 2018;28(3):176–187.
11. Kilmartin JV. Lessons from yeast: the spindle pole body and the centrosome. Philos Trans R Soc Lond B Biol Sci. 2014;369:20130456.
12. chen Lin T, Neuner A, Schiebel E. Targeting of gamma-tubulin complexes to microtubule organizing centers: conservation and divergence. Trends Cell Biol. 2014;25:296–307.
13. chen Lin T, Neuner A, Schlosser YT, Scharf AN, Weber L, Schiebel E. Cell-cycle dependent phosphorylation of yeast pericentrin regulates γ-TuSC-mediated microtubule nucleation. Elife. 2014;3:e02208.
14. Sutradhar S, Yadav V, Sridhar S, Sreekumar L, Bhattacharyya D, Ghosh SK, et al. A comprehensive model to predict mitotic division in budding yeasts. Molecular Biology of the Cell. 2015;26(22):3954–3965.
15. Yadav V, Sanyal K. Sad1 Spatiotemporally Regulates Kinetochore Clustering To Ensure High-Fidelity Chromosome Segregation in the Human Fungal Pathogen Cryptococcus neoformans. mSphere. 2018;3(4):e00190–18.

16. Yamaguchi M, Biswas SK, Kuwabara Y, Ohkusu M, Shimizu M, Takeo K. The spindle pole body of the pathogenic yeast *Cryptococcus neoformans*: variation in morphology and positional relationship with the nucleolus and the bud in interphase cells. Journal of Electron Microscopy. 2010;59(2):165–172.

17. Varshney N, Som S, Chatterjee S, Sridhar S, Bhattacharyya D, Paul R, et al. Spatio-temporal regulation of nuclear division by Aurora B kinase Ipl1 in Cryptococcus neoformans. PLoS Genet. 2019;15(2):e1007959.

18. Chatterjee S, Sarkar A, Zhu J, Khodjakov A, Mogilner A, Paul R. Mechanics of multi-centrosomal clustering in bipolar mitotic spindles. bioRxiv. 2019; p. http://dx.doi.org/10.1101/2019.12.17.879817.

19. McNally FJ. Mechanisms of spindle positioning. J Cell Biol. 2013;200(2):131–140.

20. Rasmussen CG, Humphries JA, Smith LG. Determination of Symmetric and Asymmetric Division Planes in Plant Cells. Annual Review of Plant Biology. 2011;62:387–409.

21. Kiyomitsu T, Cheeseman IM. Chromosome- and spindle- pole-derived signals generate an intrinsic code for spindle position and orientation. Nat Cell Biol. 2012;14:311–317.

22. Park DH, Rose LS. Dynamic localization of LIN-5 and GPR-1/2 to cortical force generation domains during spindle positioning. Dev Biol. 2008;315:42–54.

23. Ferenz NP, Paul R, Fagerstrom C, Mogilner A, Wadsworth P. Dynein antagonizes Eg5 by crosslinking and sliding antiparallel microtubules. Curr Biol. 2009;19(21):1833–1838.

24. Nedelec F. Computer simulations reveal motor properties generating stable antiparallel microtubule interactions. J Cell Biol. 2002;158(6):1005–15.

25. Wollman R, Civelekoglu-Scholey G, Scholey JM, Mogilner A. Reverse engineering of force integration during mitosis in the Drosophila embryo. Mol Syst Biol. 2008;4:195.

26. Rubinstein B, Larripa K, Sommi P, Mogilner A. The elasticity of motor-microtubule bundles and shape of the mitotic spindle. Phys Biol. 2009;6(1):016005.

27. Kirschner M, Mitchison T. Beyond self-assembly: From microtubules to morphogenesis. Cell. 1986;45:329–342.

28. Winey M, Bloom K. Mitotic Spindle Form and Function. Genetics. 2012;190(4):1197–1224.

29. Paul R, Wollman R, Silkworth WT, Nardi IK, Cimini D, Mogilner A. Computer simulations predict that chromosome movements and rotations accelerate mitotic spindle assembly without compromising accuracy. PNAS. 2009;106(37):15708 –15713.

30. Magidson V, Connell CBO, Lončarek J, Paul R, Mogilner A, Khodjakov A. The Spatial Arrangement of Chromosomes during Prometaphase Facilitates Spindle Assembly. Cell. 2011;146:555–567.

31. Magidson V, Paul R, Yang N, Ault JG, O'Connell CB, Tikhonenko I, et al. Adaptive changes in the kinetochore architecture facilitate proper spindle assembly. Nature Cell Biology. 2015;17:1134–1144.

32. Anderson M, Haase J, Yeh E, Bloom K. Function and assembly of DNA looping, clustering, and microtubule attachment complexes within a eukaryotic kinetochore. Mol Biol Cell. 2009;20:4131–4139.

33. Walczak CE, Cai S, Khodjakov A. Mechanisms of chromosome behaviour during mitosis. Nat Rev Mol Cell Biol. 2010;11(2):91–102.

34. Heald R, Khodjakov A. Thirty years of search and capture: The complex simplicity of mitotic spindle assembly. J Cell Biol. 2015;211(6):1103–1111.

35. Som S, Chatterjee S, Paul R. Mechanistic three-dimensional model to study centrosome positioning in the interphase cell. Phys Rev E. 2019;99:012409.

36. Lee IJ, Wang N, Hu W, Schott K, Bahler J, Thomas H Giddings J, et al. Regulation of spindle pole body assembly and cytokinesis by the centrin-binding protein Sfi1 in fission yeast. Mol Biol Cell. 2014;25(18):2735–2749.

37. Seybold C, Schiebel E. Spindle pole bodies. Current Biology. 2013;23(19):R858–R860.

38. Civelekoglu-Scholey G, Sharp DJ, Mogilner A, Scholey JM. Model of Chromosome Motility in Drosophila Embryos: Adaptation of a General Mechanism for Rapid Mitosis. Biophysical Journal. 2006;19(11):3966–3982.

39. Fink G, Schuchardt I, Colombelli J, Stelzer E, Steinberg G. Dynein-mediated pulling forces drive rapid mitotic spindle elongation in Ustilago maydis. EMBO J. 2006;25(20):4897–908.

40. Finley KR, Bouchonville KJ, Quick A, Berman J. Dynein-dependent nuclear dynamics affect morphogenesis in Candida albicans by means of the Bub2p spindle checkpoint. J Cell Sci. 2008;121:466–76.

41. Letort G, Nedelec F, Blanchoin L, Thery M. Centrosome centering and decentering by microtubule network rearrangement. Mol Biol Cell. 2016;27(18):2833–43.

42. Dogterom M, Yurke B. Measurement of the force-velocity relation for growing microtubules. Science. 1997;278(5339):856–60.

43. Soppina V, Rai AK, Ramaiya AJ, Barak P, Mallik R. Tug-of-war between dissimilar teams of microtubule motors regulates transport and fission of endosomes. Proc Natl Acad Sci USA. 2009;106(46):19381–6.

44. Muller MJI, Klumpp S, Lipowsky R. Tug-of-war as a cooperative mechanism for bidirectional cargo transport by molecular motors. Proc Natl Acad Sci USA. 2008;105(12):4609–14.

45. Markus SM, Plevock KM, Germain BJS, Punch JJ, Meaden CW, Lee W. Quantitative Analysis of Pac1/LIS1-mediated Dynein Targeting: Implications for Regulation of Dynein Activity in Budding Yeast. Cytoskeleton (Hoboken, NJ). 2011;68(3):157–74.

46. Joglekar AP, Hunt AJ. A simple, mechanistic model for directional instability during mitotic chromosome movements. Biophys J. 2002;83(1):42–58.

47. Sau S, Sutradhar S, Paul R, Sinha P. Budding yeast kinetochore proteins, Chl4 and Ctf19, are required to maintain SPB-centromere proximity during G1 and late anaphase. PLoS One. 2014;9(7):e101294.

48. Winters L, Ban I, Prelogovic M, Kalinina I, Pavin N, Tolic IM. Pivoting of microtubules driven by minus-end-directed motors leads to spindle assembly. BMC Biology. 2019; p. 10.1186/s12915–019–0656–2.

49. Bertalan Z, Budrikis Z, Porta CAML, Zapperi S. Role of the Number of Microtubules in Chromosome Segregation during Cell Division. PLOS ONE. 2015; p. 10.1371/journal.pone.0141305.

50. Wollman R, Cytrynbaum EN, Jones JT, Meyer T, Scholey JM, Mogilner A. Efficient Chromosome Capture Requires a Bias in the 'Search-and-Capture' Process during Mitotic-Spindle Assembly. Current Biology. 2005;15:828–832.

51. Sarkar A, Rieger H, Paul R. Search and Capture Efficiency of Dynamic Microtubules for Centrosome Relocation during IS Formation. Biophysical Journal. 2019;116:2079–2091.

52. Kozubowski L, Yadav V, Chatterjee G, Sridhar S, Yamaguchi M, Kawamoto S, et al. Ordered Kinetochore Assembly in the Human-Pathogenic Basidiomycetous Yeast Cryptococcus neoformans. mBio. 2013;4(5):00614–13.

53. Tubman ES, Biggins S, Odde DJ. Stochastic Modeling Yields a Mechanistic Framework for Spindle Attachment Error Correction in Budding Yeast Mitosis. Cell Systems. 2017;4:645–650.

54. Meyer RE, Kimand S, Obeso D, Straight PD, Winey M, Dawson DS. Mps1 and Ipl1/Aurora B Act Sequentially to Correctly Orient Chromosomes on the Meiotic Spindle of Budding Yeast. SCIENCE. 2013;339:1071–1074.

55. Cairo G, MacKenzie AM, Lacefield S. Differential requirement for Bub1 and Bub3 in regulation of meiotic versus mitotic chromosome segregation. J Cell Biol. 2020;219(4):e201909136.

56. Balasubramanian MK, Bi E, Glotzer M. Comparative Analysis of Cytokinesis in Budding Yeast, Fission Yeast and Animal Cells. Current Biology. 2004;14:R806–R818.

57. Kalinina I, Nandi A, Delivani P, Chacón MR, Klemm AH, Ramunno-Johnson D, et al. Pivoting of microtubules around the spindle pole accelerates kinetochore capture. Nat Cell Biol. 2013;15(1):82–87.

58. Lamson AR, Edelmaier CJ, Glaser MA, Betterton MD. Theory of Cytoskeletal Reorganization during Cross-Linker-Mediated Mitotic Spindle Assembly. Biophysical Journal. 2019;116:1719–1731.

59. Nayak I, Das D, Nandi A. Kinetochore capture by spindle microtubules: why fission yeast may prefer pivoting to search-and-capture. bioRxiv. 2019; p. http://dx.doi.org/10.1101/673723.

60. Odde DJ. Chromosome Capture: Take Me to Your Kinetochore. Current Biology. 2005;15(9):R328–R330.

61. Winey M, Mamay CL, O'Toole ET, Mastronarde DN, Giddings TH, McDonald KL, et al. Three-dimensional ultrastructural analysis of the Saccharomyces cerevisiae mitotic spindle. The Journal of Cell Biology. 1995;129(6):1601–1615.

62. Kops GJPL, Weaver BAA, Cleveland DW. On the road to cancer: aneuploidy and the mitotic checkpoint. Nature Reviews Cancer. 2005;5:773–785.

63. Rajagopalan H, Lengauer C. Aneuploidy and cancer. Nature. 2004;432:338–341.

64. Biggins S, Murray AW. The budding yeast protein kinase Ipl1/Aurora allows the absence of tension to activate the spindle checkpoint. Genes Dev. 2001;15(23):3118–3129.

65. Biggins S, Severin FF, Bhalla N, Sassoon I, Hyman AA, Murray AW. The conserved protein kinase Ipl1 regulates microtubule binding to kinetochores in budding yeast. Genes Dev. 1999;13:532–544.

66. Cheeseman IM, Anderson S, Jwa M, Green EM, Kang J, Yates JR, et al. Phospho-Regulation of Kinetochore-Microtubule Attachments by the Aurora Kinase Ipl1p. Cell. 2002;111(2):163–172.

67. Dewar H, Tanaka K, Nasmyth K, Tanaka TU. Tension between two kinetochores suffices for their bi-orientation on the mitotic spindle. Nature. 2004;428:93–97.

68. Tanaka TU, Rachidi N, Janke C, Pereira G, Galova M, Schiebel E, et al. Evidence that the Ipl1-Sli15 (Aurora Kinase-INCENP) Complex Promotes Chromosome Bi-orientation by Altering Kinetochore-Spindle Pole Connections. Cell. 2002;108(3):317–329.

69. Shaw SL, Yeh E, Maddox P, Salmon ED, Bloom K. Astral microtubule dynamics in yeast: a microtubule-based searching mechanism for spindle orientation and nuclear migration into the bud. J Cell Biol. 1997;139(4):985–994.

70. Lerit DA, Smyth JT, Rusan NM. Organelle asymmetry for proper fitness, function, and fate. Chromosome Res. 2013;21(3):271–286.

71. Pereira G, Tanaka TU, Nasmyth K, Schiebel E. Modes of spindle pole body inheritance and segregation of the Bfa1p-Bub2p checkpoint protein complex. The EMBO Journal. 2001;20(22):6359–6370.

72. Piel M, Meyer P, Khodjakov A, Rieder CL, Bornens M. The respective contributions of the mother and daughter centrioles to centrosome activity and behavior in vertebrate cells. J Cell Biol. 2000;149(2):317–30.

73. Yamashita YM, Mahowald AP, Perlin JR, Fuller MT. Asymmetric Inheritance of Mother Versus Daughter Centrosome in Stem Cell Division. SCIENCE. 2007;315:518–521.

MTOC clustering and nuclear division through proper spindle positioning in yeast: a microtubule grow-and-catch model - Supplementary Information

Saptarshi Chatterjee[1], Subhendu Som[1], Neha Varshney[2¤], Kaustuv Sanyal[2], Raja Paul[1*]

1 School of Mathematical and Computational Sciences, Indian Association for the Cultivation of Science, Kolkata -700032, India
2 Molecular Mycology Laboratory, Molecular Biology and Genetics Unit, Jawaharlal Nehru Centre for Advanced Scientific Research, Jakkur, Bangalore -560064, India
¤Current Address: Ludwig Institute for Cancer Research, Department of Cellular and Molecular Medicine, University of California San Diego, La Jolla, CA 92093, USA

* raja.paul@iacs.res.in

One-dimensional mathematical model describing the forces due to localized dynein organization in the daughter cell cortex:

In the mathematical template, we assume that the dynein density in the mother cortex is uniform as considered in the earlier scenario. However, in the daughter cortex the dyneins are spatially localized as discrete patches of length l_1 with the gap between two consecutive patches being l_2. We further assume that the effective dynein density within a patch falls exponentially with distance. Hence,

$$\lambda^D_{dyn}(s) = \lambda^D_{dyn}(0)e^{-s/\xi^D_{dyn}} \tag{1}$$

Here, $\lambda^D_{dyn}(0)$ denotes the effective dynein density at the intersection of the axis of symmetry and the daughter cortex. ξ^D_{dyn} is an external tunable parameter in the current model which dictates how the effective dynein density drops off within the patch as one moves away from the intersection of the axis of symmetry and the daughter cortex in the transverse direction along the daughter cortex. It is evident from the present model construction that the net contribution to $F^{cor(D)}_{dyn(sliding)}$ will come from the discrete patches only. Hence the integration $\int_0^{l^D_{arc}}$ will have nonzero finite contributions from $\int_0^{l_1} + \int_{l_1+l_2}^{l_2+2l_1} + ...$ only. Now the expression for $F^{cor(D)}_{dyn(sliding)}$ reads,

$$\begin{aligned}
F^{cor(D)}_{dyn(sliding)} &= B_D \int_0^{l^D_{arc}} ds\ e^{-(d+r_D-x-a+s)/L^{av}_{MT}} \lambda^D_{dyn}(s) \\
&= B_D \lambda^D_{dyn}(0) \int_0^{l^D_{arc}} ds\ e^{-(d+r_D-x-a+(1+\gamma)s)/L^{av}_{MT}} \\
&= B_D \lambda^D_{dyn}(0) \Bigg[\int_0^{l_1} ds\ e^{-(d+r_D-x-a+(1+\gamma)s)/L^{av}_{MT}} + \\
&\quad \int_{l_1+l_2}^{l_2+2l_1} ds\ e^{-(d+r_D-x-a+(1+\gamma)s)/L^{av}_{MT}} + \int_{2l_2+2l_1}^{2l_2+3l_1} ds\ e^{-(d+r_D-x-a+(1+\gamma)s)/L^{av}_{MT}} + ... \Bigg] \\
&= \frac{B_D \lambda^D_{dyn}(0) L^{av}_{MT}}{(1+\gamma)} e^{-(d+r_D-x-a)/L^{av}_{MT}} \Bigg[1 - e^{-(1+\gamma)l_1/L^{av}_{MT}} + e^{-(1+\gamma)(l_1+l_2)/L^{av}_{MT}} \\
&\quad - e^{-(1+\gamma)(l_2+2l_1)/L^{av}_{MT}} + e^{-(1+\gamma)(2l_2+2l_1)/L^{av}_{MT}} - e^{-(1+\gamma)(2l_2+3l_1)/L^{av}_{MT}} + ... \Bigg]
\end{aligned} \tag{2}$$

In the above expressions we take, $L^{av}_{MT}/\xi^D_{dyn} = \gamma \implies 1/\xi^D_{dyn} = \gamma/L^{av}_{MT}$. Let us reconstruct the above expression for $F^{cor(D)}_{dyn(sliding)}$ by taking,

$$e^{-(1+\gamma)l_1/L^{av}_{MT}} = \mathcal{P} \tag{3}$$

$$e^{-(1+\gamma)l_2/L^{av}_{MT}} = \mathcal{Q} \tag{4}$$

Plugging $\mathcal{P}$ and $\mathcal{Q}$ into the expression of $F^{cor(D)}_{dyn(sliding)}$ we obtain,

$$\begin{aligned} F^{cor(D)}_{dyn(sliding)} &= \frac{B_D \lambda^D_{dyn}(0) L^{av}_{MT}}{1+\gamma} e^{-(d+r_D-x-a)/L^{av}_{MT}} \\ &\quad \left[1 - \mathcal{P} + \mathcal{P}\mathcal{Q} - \mathcal{P}^2\mathcal{Q} + \mathcal{P}^2\mathcal{Q}^2 - \mathcal{P}^3\mathcal{Q}^2 + ...\right] \\ &= \frac{B_D \lambda^D_{dyn}(0) L^{av}_{MT}}{1+\gamma} e^{-(d+r_D-x-a)/L^{av}_{MT}} \left[1 - \mathcal{P}(1-\mathcal{Q})\frac{1-(\mathcal{P}\mathcal{Q})^n}{1-\mathcal{P}\mathcal{Q}}\right] \end{aligned} \tag{5}$$

where $nl_1 + nl_2 \simeq nl_1 + (n-1)l_2 \simeq l^D_{arc}$. Furthermore, only retaining terms up to first order we obtain,

$$F^{cor(D)}_{dyn(sliding)} = \frac{B_D \lambda^D_{dyn}(0) L^{av}_{MT}}{1+\gamma} e^{-(d+r_D-x-a)/L^{av}_{MT}} \left[1 - e^{-(1+\gamma)l_1/L^{av}_{MT}}\right] \tag{6}$$

It is evident from the above equation that putting $\gamma = 0$ and $l_1 = l^D_{arc}$, we get back the earlier expression with uniform dynein density.

Steric Forces

We have considered steric hindrance between the cell membrane and the spindle. The steric clash between the cell membrane and the spindle is devised via the hardcore repulsion between cell membrane in the mother bud and $SPB(L)$, and between the cell membrane in the daughter bud and $SPB(R)$. The steric repulsion in the mother bud $F^{steric(M)}_{cell-mem}$ is taken as

$$F^{steric(M)}_{cell-mem} = C_M e^{-\zeta_M (R_M + x - a)/L^{av}_{MT}} \tag{7}$$

Similarly, the steric repulsion in the daughter bud $F^{steric(D)}_{cell-mem}$ is

$$F^{steric(D)}_{cell-mem} = C_D e^{-\zeta_D (d + r_D - x - a)/L^{av}_{MT}} \tag{8}$$

We take $C_M = C_D$ and $\zeta_M = \zeta_D$ since the repulsive forces stemmed at both the mother and daughter cell-membrane upon steric interaction are identical in nature. From the expression, it is also clear that the magnitude of the force solely depends upon the instantaneous overlap between the objects under consideration. Here C_M and C_D refer to the amplitudes of the forces generated due to the steric clashes between cell membrane (mother or daughter) and $SPB(L$ or $R)$. The length scale, more precisely, the short-range limit of the steric forces is governed by ζ_M and ζ_D. As ζ_M (or ζ_D) with nonzero positive value is levelled up, $F^{steric(M \text{ or } D)}_{cell-mem}$ drops sharply with increasing distance.

To include the effect of the finite size of the $SPB(L$ or $R)$ (r_{SPB}), in the steric force expressions R_M is replaced by $R_M \to R_M - r_{SPB}$ and r_D is replaced by $r_D \to r_D - r_{SPB}$ where r_{SPB} is the radius of the SPB.

Model Assumptions

The mathematical model construction is based upon several simplifications described in the following: 1. The model does not account for the process of bi-orientation on the NE. We assume a bi-oriented configuration of two SPBs throughout. 2. The spindle length is fixed and taken to be $2a$ across the whole range of spatial variation along the axis of symmetry. 3. The motion of the nucleus/ spindle is strictly confined along the X-axis. We only emphasize the translational motion of the spindle of length $2a$ governed by a set of MT mediated forces. The rotational degrees of freedom responsible for the spindle orientation is not considered in the model for simplicity. The spindle is always laid upon the X-axis with its orientation being parallel to the symmetry axis (X-axis). Restricting the spindle movement along the axis of symmetry by default accounts for the net cancellation of forces along the transverse direction since MT nucleation is considered isotropic in all directions. 4. We ignore stochastic fluctuations originating from the randomness in MT dynamics in the force balance landscape while the governing forces are evaluated in a time-independent quasi-equilibrium configuration. 5. For simplicity, we have not considered a load-dependent variation of average MT length in the analytical model. However, in the agent-based simulation, load-dependent modulation of the following MT dynamic instability parameters, growth velocity (v_g) and catastrophe frequency (f_c) have been taken into account.

The above-mentioned assumptions in the mathematical prescription do not alter the overall qualitative attributes of the spindle positioning.

Additional numerical analysis of the analytical model

Instantaneous push from the mother and the daughter cortex forces the spindle to localize in mother bud

From the analytical model geometry (S2 Fig) and S4 FigA, it is clear that the instantaneous push from the mother and the daughter cortex are oppositely directed. In the expressions for the instantaneous pushing forces $F^{cell-mem(M)}_{push-inst}$ and $F^{cell-mem(D)}_{push-inst}$, the percentage of MTs experiencing instantaneous cortical push is determined by A_M and A_D respectively. We varied this percentage as a tunable parameter of the system with the pre-imposed constraint $A_M = A_D$ for this particular case. Since the daughter bud size is smaller than the mother bud, the balancing act between these two competing forces leads to a stable spindle position inside the mother bud (S4 FigA). A configuration with equal mother and daughter bud size would lead to a stable spindle position at the center of the septin ring. Importantly, due to the very nature of the force which pushes the $SPB(L$ and/or $R)$ away from the cell membrane mother and/or daughter, in the resultant force balance landscape, only stable fixed points of the spindle position appear (S4 FigA).

In the sole presence of cortical pull from mother and daughter, spindle collapses onto the cortex

The sole presence of cortical pull from the mother and daughter cortex gives rise to unstable fixed points of the spindle position in the force balance contour for various spindle positions. In a parameter space mapped by λ^M_{dyn}= 4.0 μm $^{-1}$, λ^D_{dyn} = 5.0 μm^{-1}, we varied $B_M(= B_D)$ and observed that stable fixed points of the spindle position in the mother and daughter cortex with a slew of unstable fixed points sandwiched in between (S4 FigB). The unstable fixed points of the spindle close to the septin ring indicate that either the spindle collapses onto the mother cortex or the daughter cortex while slightly displaced from the unstable fixed point of the spindle position depending upon the direction of perturbation.

Tug of war between cortical push and pull leads to a collapse of the spindle onto the cortex

We first consider a theoretical mechanistic framework, where force transduction only either from the mother cortex or the daughter cortex is allowed. In that construction, we observe a sharp spatial transition of the spindle from the daughter (mother) cortex to mother (daughter) cortex upon step-wise increase in dynein density in mother (daughter) cortex as depicted in S4 FigC (relevant parameters: A_M = 5 pN, A_D = 5 pN, B_M = 5 pN, B_D = 5 pN, wherever applicable). Next, we carried out a sensitivity analysis in a scenario where the instantaneous cortical push and dynein mediated cortical pull stemming from both the mother and daughter cortex are present (Fig 2B, S4 FigD). We varied the dynein density in the mother cortex λ^M_{dyn} keeping the dynein density in the daughter cortex λ^D_{dyn} fixed at 5.0 μm^{-1} and vice versa (D_M=D_D=0; other parameters fixed at base values as shown in Table 1). The force balance showcases that for lower values of dynein density in the mother cortex, cortical pull from the daughter (λ^D_{dyn} fixed at 5.0 μm^{-1}) paired with the instantaneous push from the mother bud dominate leading to a spatial collapse of the spindle onto the daughter cortex marked by the stable fixed points of the spindle position in the daughter cortex. As the dynein density in the mother cortex (λ^M_{dyn}) is gradually increased, cortical pull from the mother cortex takes the driver's seat. Subsequently, the dominant cortical pull from the mother cortex initiates a spatial transition of the spindle to the mother cortex via a string of unstable fixed points of the spindle position marked by the oblique segment of the 'Z' contour (S4 FigD). Similarly, when dynein density in the mother cortex (λ^M_{dyn}) is kept fixed at 5 μm^{-1} and dynein density in the daughter cortex (λ^D_{dyn}) is varied, we observe a spatial collapse of the spindle onto the daughter cortex at higher values of λ^D_{dyn} with an intermediate regime having three fixed points of the spindle position (stable fixed points at the mother and the daughter cortex with unstable fixed points wedged in between) as discernible in the inverted 'Z' contour (Fig 2B). We also obtain fixed point contour of the spindle position having stable fixed points at the mother and daughter cortex with unstable fixed points located in between when average MT length (L^{av}_{MT}) is varied (S4 FigE) keeping other relevant parameters fixed (Table 1 and λ^M_{dyn} = 5 μm^{-1}, λ^D_{dyn} = 10 μm^{-1}).

Combination of MT buckling with cortical push and pull prevents collapse, maintains stable spindle position near septin ring

Allowing force transduction solely either from the mother cortex or the daughter cortex in presence of MT buckling, the stable fixed points of the spindle position make a spatial transition toward the mother (daughter) cortex from the daughter (mother) cortex upon a gradual increase in cortical dynein density λ_{dyn}^{M} or λ_{dyn}^{D} (S4 FigF). It is imperative to note that unlike previous scenarios, in presence of MT buckling, the spindle does not collapse onto the cortical region, rather localizes $\simeq 1$ μm away from the cortex (S4 FigF). It is evident from the expression of the buckling forces $F_{buckle}^{cor(M)}$ and $F_{buckle}^{cor(D)}$ that in the vicinity of the cortex the force generated due to MT buckling shoots up to a very high value. Since the force due to MT buckling is of 'pushing' nature, it pushes the spindle away from the cortex, thus preventing the spindle from collapsing onto the cortex. In presence of MT buckling transition in both the mother and daughter cortex, the balancing act between the governing forces ($F_{push-inst}^{cell-mem(M \text{ and } D)}$, $F_{dyn}^{cor(M \text{ and } D)}$, $F_{buckle}^{cor(M \text{ and } D)}$), leads to a stable positioning of the spindle within the daughter bud in the vicinity of the septin ring (Fig 2C-2D). We observed that upon step-wise increment in the dynein density within the daughter cortex (λ_{dyn}^{D}), the stable fixed point contour of the spindle position tend to shift deep inside the daughter cortex owing to an enhancement in the net force directed toward the daughter cortex as shown in Fig 2C (relevant parameters: $\lambda_{dyn}^{M} = 3.0$ μm^{-1}, other parameters as in Table 1). We also carried out sensitivity analysis on the robustness of the stable spindle positioning close to the septin ring within the daughter bud upon variation in the average MT length (L_{MT}^{av}). We find that across a reasonably significant range of L_{MT}^{av} values, the location of the stable fixed point for the spindle remains unperturbed within the daughter bud (Fig 2D, relevant parameters: $\lambda_{dyn}^{M} = 3.0$ μm^{-1}, $\lambda_{dyn}^{D} = 10.0$ μm^{-1}, other parameters as in Table 1).

Differential spatial arrangement of dyneins in mother and daughter cortex results in force balance landscape with stable as well as unstable positions of the spindle

Our previous study [1] indicates that the spatial arrangement of dyneins in the mother and daughter cortex is different. The dynein puncta in the mother cortex are uniformly distributed, whereas in the daughter cortex a large localized dynein punctum near the axis of symmetry is observed. This differential spatial arrangement alludes to the fact that for proper nuclear migration (e.g. proper spindle positioning) a directed pull from the daughter cortex on the nucleus is crucial to navigating the nucleus inside the daughter bud. Further, we also observed that irrespective of whether the cortical milieu is enriched with uniform dynein distribution at both the mother and the daughter cortex or the differential distribution as mentioned above, the innate mechanistic perspective relies upon the net pulling force generation from the daughter cortex. This leads to a question that how the force balance landscape governing the spindle positioning behaves when one makes a gradual transition from localized puncta in the daughter cortex to a full-fledged uniform distribution. To address that we assign a characteristic length scale ξ_{dyn}^{D} with the effective localized dynein puncta within the daughter cortex. As ξ_{dyn}^{D} is increased, the effective spatial profile of dyneins within the daughter cortex makes a gradual changeover to a uniform distribution. With this mathematical template at hand, we carried out sensitivity analysis on the force balance landscape governed by various MT mediated forces (e.g. instantaneous push, dynein pull, MT buckling transition) upon the variation in the parameter ξ_{dyn}^{D}. In presence of instantaneous push and dynein pull from the daughter (with no force transduction from the mother cortex and no MT buckling), the gradual increment in ξ_{dyn}^{D} leads to an enhancement in the dynein pull from the daughter invoking a spatial changeover of the spindle from the mother cortex to the daughter cortex via a slew of unstable fixed points of the spindle position (S4 FigG). For lower values of ξ_{dyn}^{D}, instantaneous push dominates the force balance landscape shoving the spindle onto the mother cortex (marked by the stable fixed-point contour of the spindle position in the mother cortex). Furthermore, in presence of instantaneous push and dynein pull from both the mother and the daughter cortex, the variation in ξ_{dyn}^{D} yields null force contours (the inverted 'Z' contour) having stable fixed points of the spindle position at the mother and the daughter cortex and a string of unstable fixed points of the spindle location sandwiched in between (S4 FigH). The gradual increase in ξ_{dyn}^{D} leads to stable fixed points of the spindle position inside the daughter cortex, around ~ 0.8 μm away from the septin ring when instantaneous push, dynein pull and MT buckling at both the mother and daughter cortex act alongside each other (S4 FigI). Stable spindle positioning at higher values of ξ_{dyn}^{D} (referring to the uniformity within the spatial organization of dyneins) further corroborates with the 'agent-based' simulation which includes uniform distribution of dyneins in both mother and daughter cortex as depicted in S3 FigB, S3 FigE (fourth bar) and S4 FigI.

Modeling the influence of chemical concentration on MT grow and catch in kinetochore capture

We assume that the spatial profile of the chemical concentration ($n(r)$) decays down exponentially as one moves away from the KT precluster. Hence the chemical concentration $n(r)$ can be written as,

$$n(r) = \lambda e^{-\frac{r}{\zeta r_{cluster}}} \tag{9}$$

where λ denotes the strength of the chemical concentration, $r_{cluster}$ is the distance of the SPBs from the KT precluster and r is also measured from the KT precluster. We also assume that in this particular mechanism under consideration, the catastrophe frequency of the MTs exponentially depends upon the local concentration of the chemical signal in the following manner.

$$f_c = f_{c0}e^{-n(r)} = f_{c0}e^{-\lambda e^{-\frac{r}{\zeta r_{cluster}}}} = f_{c0}e^{-\lambda\left(1-\frac{r}{\zeta r_{cluster}}\right)} \tag{10}$$

Under the assumption $\lambda \sim 1$,

$$f_c = f_{c0}e^{-\left(1-\frac{r}{\zeta r_{cluster}}\right)} = f_{c0}\frac{r}{\zeta r_{cluster}} \tag{11}$$

f_{c0} is chosen to be the catastrophe frequency base value as denoted in Table 1.

Modeling the consequence of chemical gradient dependent catastrophe on MT grow and catch in kinetochore capture

The spatial concentration profile is taken as,

$$n_r = \lambda e^{-\frac{r}{\zeta r_{cluster}}} \tag{12}$$

The change in concentration between two points at distance r_1 and r_2 (measured from the KT precluster) is $\triangle n$ where,

$$\begin{aligned} \triangle n &= n(r_1) - n(r_2) = \lambda\left(1 - \frac{r_1}{\zeta r_{cluster}}\right) - \lambda\left(1 - \frac{r_2}{\zeta r_{cluster}}\right) \\ &= -\frac{\lambda}{\zeta r_{cluster}}(r_1 - r_2) = -\frac{\lambda}{\zeta r_{cluster}}\triangle l \end{aligned} \tag{13}$$

Here $\triangle l$ accounts for the projection of the relative distance between two points from the KT precluster. Now we introduce the dependence of the MT catastrophe frequency on the chemical gradient $\triangle n$ in the following manner.

$$f_c = f_{c0}e^{\triangle n} = f_{c0}e^{-\frac{\lambda}{\zeta r_{cluster}}\triangle l} \tag{14}$$

We further rescale $\frac{\lambda}{\zeta r_{cluster}}$ as $\frac{\lambda'}{v_g \triangle t}$ where $v_g \triangle t = l_0$ and λ'=10. Hence, the expression for MT catastrophe frequency becomes,

$$f_c = f_{c0}e^{-\frac{\lambda' \triangle l}{l_0}} \tag{15}$$

We compute the change in chemical concentration ($\triangle n$) around a growing MT tip during two successive time steps. It is evident that this change is proportional to the change in relative distance of the MT tip from the KT precluster between two successive time steps. The length increment of an elongating MT within two successive time steps is $v_g \triangle t$. Hence, the maximum change in the relative distance of a growing MT tip from the center of the KT precluster between two consecutive timesteps is $l_0 = v_g \triangle t$, which we used as the rescaling factor in the expression of catastrophe frequency. From the expression of catastrophe frequency, we glean that a MT growing toward the KT precluster is less likely to undergo catastrophe whereas a elongating 'misdirected' MT (MT trajectory deviating away from the KT precluster) is more likely to make a transition to the shrinking state owing to a gradient dependent enhanced catastrophe frequency. This modulated catastrophe frequency is adequate to render focused MT beams toward the KT precluster. Here, f_{c0} is chosen to be the catastrophe frequency base value as denoted in Table 1.

Reference

[1] N. Varshney, S. Som, S. Chatterjee, S. Sridhar, D. Bhattacharyya, R. Paul, and K. Sanyal, PLoS Genet **15(2)**, e1007959 (2019).